

1 **High frequency, continuous measurements reveal strong diel and seasonal cycling of**
2 **$p\text{CO}_2$ and CO_2 flux in a mesohaline reach of the Chesapeake Bay**

3
4

5 **A. Whitman Miller^{1*}, Jim R. Muirhead¹, Amanda C. Reynolds¹, Mark S. Minton¹ and Karl**
6 **J. Klug¹**

7 ¹Smithsonian Environmental Research Center, Edgewater, MD USA

8

9 Corresponding author: A. Whitman Miller (millerw@si.edu)

10 †Additional author notes should be indicated with symbols (current addresses, for example).

11 **Key Points:**

- 12 • Automated $p\text{CO}_2$ measurements capture daily cycles and anomalous events in estuaries
13 where $p\text{CO}_2$ changes rapidly and across a wide range.
- 14 • Rhode River is net autotrophic (Dec-May), net heterotrophic (Jun-Nov), NEP is near
15 balanced annually, but can reverse status during a single day.
- 16 • Year-round continuous measurements reveal that $p\text{CO}_2$ and CO_2 flux are mediated by
17 temperature effects on biological activity and are inverse to the physical solubility of
18 CO_2 .

19

20

21 ABSTRACT

22 We estimated hourly air-water gas transfer velocities (k_{600}) for carbon dioxide in the Rhode
23 River, a mesohaline subestuary of the Chesapeake Bay. Gas transfer velocities were calculated
24 from estuary-specific parameterizations developed explicitly for shallow, microtidal estuaries in
25 the Mid-Atlantic region of the United States, using standardized wind speed measurements.
26 Combining the gas transfer velocity with continuous measurements of $p\text{CO}_2$ in the water and in
27 the overlying atmosphere, we determined the direction and magnitude of CO_2 flux at hourly
28 intervals across a 3 yr record (01 July 2018 to 01 July 2021). Continuous year-round
29 measurements enabled us to document strong seasonal cycling whereby the Rhode River is
30 primarily autotrophic during cold-water months (Dec–May), and largely net heterotrophic in
31 warm-water months (Jun–Nov). Although there is inter-annual variability in CO_2 flux in the
32 Rhode River, the annual mean condition is near carbon neutral. Measurement at high temporal
33 resolution across multiple years revealed that CO_2 flux and apparent trophic status can reverse
34 during a single 24 hr period. $p\text{CO}_2$ and CO_2 flux are mediated by temperature effects on
35 biological activity and are inverse to temperature-dependent physical solubility of CO_2 in water.
36 Biological/biogeochemical carbon fixation and mineralization are rapid and extensive, so
37 sufficient sampling frequency is crucial to capture unbiased extremes and central tendencies of
38 these estuarine ecosystems.

39

40 1. Introduction

41 Understanding the air–sea exchange of gases and establishing methodologies for accurate
42 measurements has been a decades-long focus of atmospheric scientists, oceanographers, and
43 biogeochemists seeking to understand interactions between oceans and the atmosphere and how
44 these interactions contribute to the global carbon cycle (Broecker et al., 1979; Wanninkhof,
45 1992, 2013). Coastal oceans and estuaries are ecosystems of interest for understanding the
46 complex nature and contribution of the land–sea interface to lateral mass transport of carbon
47 (Abril & Borges, 2005; Cai & Wang, 1998; Frankignoulle et al., 1998; Song et al., 2023) but also
48 with respect to the role these ecosystems play as both atmospheric CO_2 sources and sinks (Abril
49 & Borges, 2005; Chen et al., 2020; Dai et al., 2022; Jiang et al., 2008). The exchange of carbon
50 dioxide, methane, and other greenhouse gases (GHGs) between Earth’s atmosphere and inland
51 waters, estuaries, coastal oceans are well-documented but not fully quantified (Abril & Borges,

52 2005; Cai, 2011; Laruelle et al., 2017; Raymond & Cole, 2001; Raymond et al., 2013; Van Dam
53 et al., 2019). CO₂ evasion from estuaries alone has been estimated at 15–17% of the total CO₂
54 input from oceans to the atmosphere (Chen et al., 2020; Laruelle et al., 2017), indicating the
55 regional and global significance of estuaries (Bauer et al., 2013; Frankignoulle et al., 1998; Jiang
56 et al., 2008). Yet, there is still great uncertainty surrounding the true net contributions of coastal
57 oceans, estuaries, and inland water bodies to the atmospheric loading of GHGs (Borges, 2005;
58 Chen et al., 2020; Herrmann et al., 2020; Joesoef et al., 2015; Laruelle et al., 2017; Raymond et
59 al., 2013; Van Dam et al., 2019).

60
61 To better understand the effects of estuaries on atmospheric GHG exchange and accumulation, it
62 is imperative that we understand their capacity and function as carbon sources and sinks and
63 ultimately how estuaries factor into the planet's overall global carbon budget (Herrmann et al.,
64 2020; Laruelle et al., 2017; Van Dam et al., 2019). Many attempts to characterize CO₂ flux in
65 estuaries and nearshore oceans (Chen et al., 2013; Herrmann et al., 2020; Rosentreter et al. 2021)
66 have relied on direct measurements using floating domes, tracer gases or, more recently, eddy
67 covariance methods (Laruelle et al., 2017; Van Dam et al., 2019). Because flux measurements are
68 time intensive, they tend to be temporally and spatially limited (Herrmann et al., 2020; Klaus &
69 Vachon, 2020). Using direct flux measurements to derive accurate gas transfer velocity
70 constants (K_o , the velocity of gas crossing the air-water boundary) enables models to be
71 parameterized to estimate K_o and compute gas flux. Thus, correlative models that incorporate
72 simultaneous environmental measurements such as wind and/or water velocity, factors that affect
73 turbulence at the air-water interface and promote gas exchange, have aided in the widespread
74 accumulation of gas flux estimates (Raymond & Cole, 2001; Van Dam et al., 2019; Wanninkhof,
75 2014). Gas transfer velocity constant models vary according to the habitat/system being observed
76 and chemical, physical, and biological factors present in each (e.g., lakes, rivers/streams,
77 estuaries, and oceans; Herrmann et al., 2020; Ho et al., 2016; Raymond & Cole, 2001; Van Dam
78 et al., 2019; Wanninkhof, 1992). To reduce uncertainty of computed gas fluxes, it is critical that
79 the appropriate K_o models are matched to a targeted ecosystem.

80
81 Coastal oceans and estuaries are exceptionally complex, frequently characterized by their relative
82 shallowness and how their freshwater inputs (riverine, surface, and groundwater) mix with salt

83 water (Chen et al., 2020). High nutrient and pollutant loading, due to urbanization and
84 eutrophication by humans, also have important effects on estuaries and coastal oceans (Freeman
85 et al., 2019). High spatial and temporal variability are hallmarks of estuaries.

86
87 Here we present a 3 year data set that combines high frequency (1 min interval) measurements of
88 dissolved and atmospheric CO₂ with co-located and continuous measurements of salinity, water
89 temperature, tidal cycling, and wind velocity, recorded at the Smithsonian Environmental
90 Research Center (SERC) dock, in the Rhode River, Maryland. To estimate hourly, daily,
91 seasonal, and annual CO₂ flux rates, we applied a CO₂ gas velocity constant model developed by
92 Van Dam et al. (2019) for the New River, North Carolina. This model is expressly designed for
93 application to shallow, well-mixed, microtidal estuaries located in the Mid-Atlantic coast of the
94 United States.

95

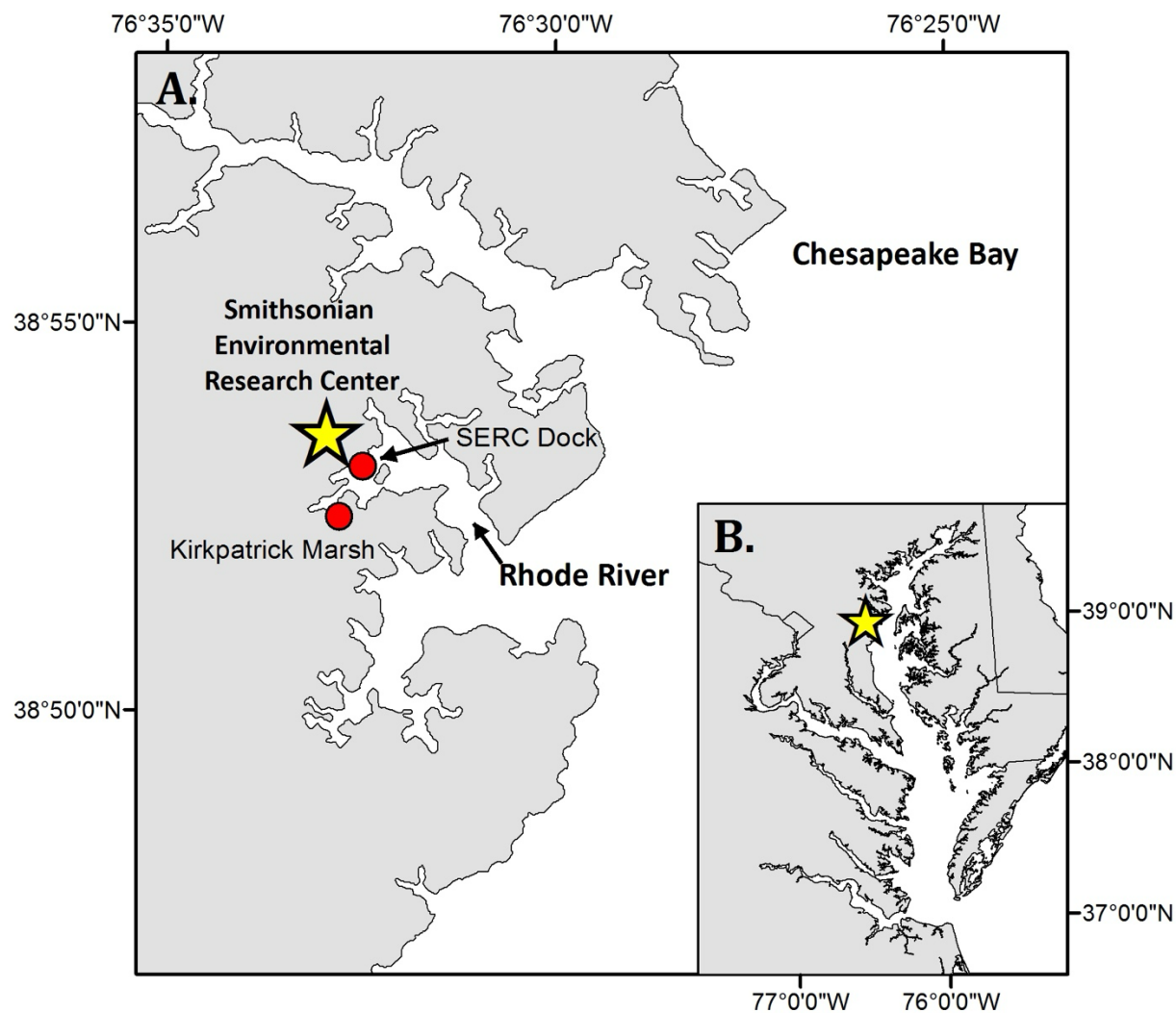
96 **2. Methods**

97 2.1 Study Location

98 The Rhode River is a tributary and subestuary of the Chesapeake Bay, a drowned river valley,
99 coastal plain estuary (Fig. 1). The Rhode River has been studied extensively by SERC staff and
100 colleagues for over 4 decades: nutrient chemistry (Jordan & Correll, 1991; Jordan et al., 1991),
101 phytoplankton ecology (Gallegos et al., 2010), color dissolved organic matter distribution
102 (Tzortziou et al., 2008; Tzortziou et al., 2011), and more recently, modeling of dissolved organic
103 carbon (DOC) input from freshwater and tidal marsh sources (Clark et al., 2020). Located on the
104 Bay's northwestern shore (38°52'N, 76°32'W), the Rhode River is bounded at its head by Muddy
105 Creek and at its mouth by the mainstem of the Chesapeake Bay. The Rhode River is a shallow
106 (mean depth = 2 m, max depth = 4.1 m), mesohaline (0 to 18 ppt), well-mixed, eutrophic
107 tributary with a length of approximately 5 km; its surface area is approximately 5 km² with a
108 shoreline perimeter of 39 km (Breitburg et al., 2008; Clark et al., 2018). A 0.21 km² tidal marsh
109 (Kirkpatrick Marsh) fringes the estuary at the mouth of Muddy Creek (Fig. 1). Tides are semi-
110 diurnal with a mean amplitude of approximately 30 cm, but water height can be strongly affected
111 by wind and weather events. Muddy Creek is the main freshwater source of the Rhode River and
112 has a maximum flow rate of 10.42 m³ · s⁻¹ and mean flow rate 0.18 m³ · s⁻¹ (mean flow = 15,552
113 m³ · d⁻¹; Clark et al., 2020; Clark et al., 2018; Jordan et al., 1986). The mean daily volume of

114 freshwater inflow from Muddy Creek is approximately 0.5% of the mean daily tidal exchange
115 volume, based on the Rhode River's area and mean tidal amplitude. In the absence of
116 measurements of the pH or $p\text{CO}_2$ of the freshwater entering the Rhode River from Muddy Creek
117 or other lesser freshwater inputs to the estuary, we are unable to report these $p\text{CO}_2$ or pH values.
118 However, given the exceedingly small overall volume of freshwater input to the Rhode River
119 from its surrounding watershed, it is not considered a river-dominated estuary so is not expected
120 to be substantially influenced by the chemical characteristics of this input. This is not to say there
121 is no freshwater influence, only that such influences are likely quite local when mixing with far
122 larger volumes of water from the Chesapeake Bay and therefore beyond the resolution of this
123 study.

124
125 Although the Rhode River is a model ecosystem that has been studied intensively for several
126 decades across many dimensions (Clark et al. 2018; Correll et al., 1992; Gallegos et al., 1992;
127 Jordan et al. 1991; Rose et al. 2019), no work to date has expressly characterized the nature and
128 dynamics of CO_2 flux between the river and the atmosphere.



129
 130 **Fig. 1.** Location of study site on the Rhode River, Edgewater MD (A), as situated in the
 131 Chesapeake Bay (B). All $p\text{CO}_2$ and related water quality values reported were measured from the
 132 SERC dock, that extends approximately 75 m from shore on Rhode River. Red circles indicate
 133 location of dock and a tidal creek that drains the Kirkpatrick saltmarsh (marsh area = 0.21 km², 1
 134 km up estuary from the dock).
 135

136 2.2 *In Situ* Measurements, Calculated Parameters and Quantities

137 Continuous, automated environmental measurements were made in and above the Rhode River
 138 during a 3 year period between 01 July 2018 and 01 July 2021. The purpose of these

139 measurements was to document fluctuations in aqueous $p\text{CO}_2$ on a fine time scale, from which
 140 CO_2 flux between the water and atmosphere could be calculated.

141 2.2.1 Aqueous CO_2 ($p\text{CO}_{2\text{water}}$)

142 To measure the CO_2 gradient ($\Delta C = p\text{CO}_{2\text{water}} - p\text{CO}_{2\text{air}}$) across the Rhode River surface waters
 143 and its overlying atmosphere, measurements of $p\text{CO}_2$ were made with a non-dispersive infrared
 144 (NDIR) detector. In the case of dissolved gas measurements, water was equilibrated continuously
 145 with a spherical falling film equilibrator (Miller et al. 2019). Water from 1 m below the water's
 146 surface was pumped and dispersed continuously over a 25.4 cm diameter sphere. The falling film
 147 created on the sphere generates a gas exchange surface which forces CO_2 in the equilibrator
 148 headspace into equilibrium with the water's CO_2 content (i.e. mole fraction = $x\text{CO}_2$ ($\mu\text{mol/mol}$)).
 149 Water exits the equilibrator via an airtight drain that prevents headspace contamination from
 150 surrounding atmospheric air. Headspace gas circulates continuously in a closed loop through the
 151 equilibrator, water trap and gas dehumidifier, past the NDIR, and back into the equilibrator.
 152 Experimental observations concluded that spherical falling film equilibrators achieve 99%
 153 equilibration of CO_2 within 10–15 mins, depending on whether step changes are from low to
 154 high or high to low; details of the operation and performance of the falling film equilibrator are
 155 described in Miller et al. (2019). Measurements were made at 1 min intervals at a pressure equal
 156 to the ambient barometric pressure.

157
 158 Measured raw CO_2 mole fractions ($\mu\text{mol/mol}$) were converted to partial pressures (μatm) using
 159 equation 1. Minute-over-minute values were rounded down to the nearest hour and averaged to
 160 provide hourly means. The mole fractions were then evaluated with corresponding water
 161 temperature and salinity measurements following the methodology of Zeebe and Wolf-Gladrow
 162 (2001) where saturation vapor pressure of water is calculated according to Weiss and Price
 163 (1980) to determine $p\text{CO}_{2\text{water}}$.

164

$$165 \quad p\text{CO}_{2\text{water}} = x\text{CO}_2 \cdot (p - p\text{H}_2\text{O}) \quad (1)$$

166

167 where

168 $p\text{CO}_2$ = partial pressure of CO_2 of water (μatm)

169 $x\text{CO}_2$ = mole fraction of CO_2 in water ($\mu\text{mol/mol}$)

170 $p = \text{total pressure} = 1 \text{ atm}$

171 $p_{\text{H}_2\text{O}} = \text{saturation vapor pressure of water } (\mu\text{atm})$

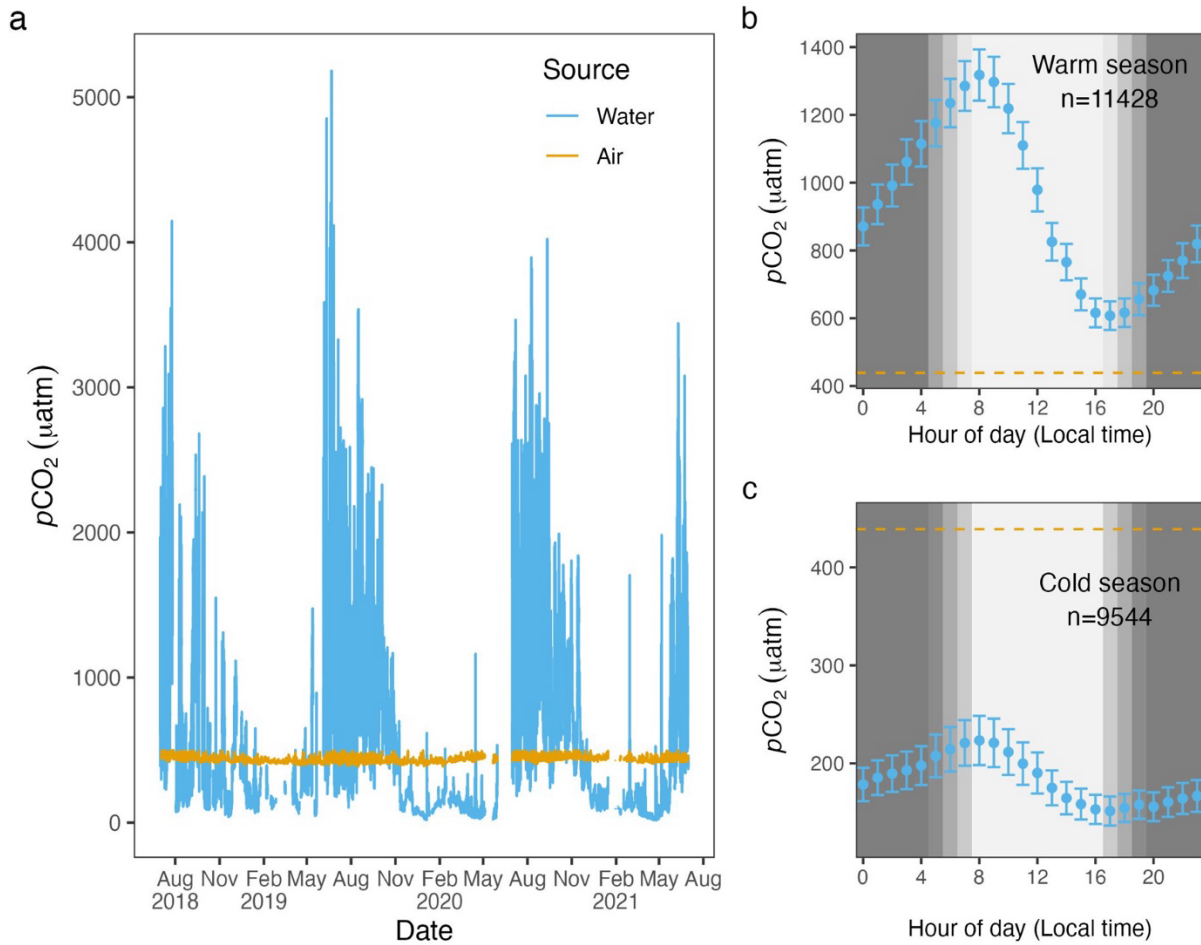
172

173 2.2.2 Atmospheric CO₂

174 Every six hours, the sample gas stream was automatically diverted with programmed solenoid
175 control valves from the equilibrator to an atmospheric port located approximately 5 m above the
176 pier deck. During atmospheric sampling, 15 1-min interval measurements were made. To
177 account for inaccuracies during the transition period from equilibrator to atmospheric sampling,
178 the final eight measurements were averaged and the first seven were discarded. Similarly, the
179 first 30 measurements following switchover from atmospheric port to equilibrator were
180 discarded, to ensure measurements were fully equilibrated with water. For these atmospheric
181 measurements, the contribution of the vapor pressure of water to the total atmospheric pressure
182 of the open-air environment was considered negligible (i.e. $p_{\text{H}_2\text{O}} = 0$ and $p = 1$), such that
183 $p\text{CO}_{2\text{atm}} = x\text{CO}_{2\text{atm}}$. As such, any potential differences are expected to fall well within the
184 measurement accuracy of the instrument (see below).

185

186 One advantage to using a shared NDIR sensor for aquatic and atmospheric samples is that any
187 minor effects of instrument drift will be reflected in both data streams, as opposed to two sensors
188 that drift independently of one another. Likewise, significant and sustained deviation from
189 typical local atmospheric variability will be captured during atmospheric sampling and can signal
190 the need for recalibration and assist with QA/QC of corresponding data from both streams. A
191 disadvantage of using a common sensor for both dissolved and atmospheric CO₂ measurements
192 is that it results in a mismatch in sampling frequency of the two. With this limitation in mind, we
193 chose a higher sampling frequency for aquatic measurements to better describe the inherently
194 higher variability in dissolved CO₂ in water vs. that in the atmosphere (Fig. 2).



195

196 **Fig. 2.** Hourly $p\text{CO}_{2\text{water}}$ (blue) and $p\text{CO}_{2\text{air}}$ (goldenrod) values from 01 July 2018 to 01 July
 197 2021 (panel a). The air-water CO_2 gradient, $\Delta C = p\text{CO}_{2\text{water}} - p\text{CO}_{2\text{air}}$ describes the directionality
 198 of gas diffusion. Negative ΔC values ($p\text{CO}_{2\text{water}}$ values falling below goldenrod demarcation)
 199 represent gas movement from air to water and vice versa. Panels b and c depict mean $p\text{CO}_{2\text{water}}$
 200 values (95% CI) for each hour of the day for warm and cold seasons, with the dashed lines equal
 201 to the mean 3 yr value of $p\text{CO}_{2\text{air}}$.

202

203 Given the 3 yr time series and strong diel cycling of $p\text{CO}_{2\text{water}}$ (and dissolved oxygen (DO), see
 204 Figs. S1 and S2) in the Rhode River, we chose to aggregate aqueous minute-over-minute
 205 measurements to mean hourly averages. Owing to the relative lack of short-term variability in
 206 local atmospheric CO_2 concentrations (Fig. 2), we used linear interpolation to impute
 207 atmospheric CO_2 concentrations during hours in between actual readings (6 hr gaps between
 208 atmospheric measurements), which we assumed to be more realistic and reliable than Last
 209 Observation Carried Forward (LOCF) methods, where the last observation is repeated for all
 210 gaps until the next measurement is encountered, a method that has fallen out of favor, especially

211 for environmental time series data (Lachin, 2016). To determine if any inadvertent bias was
212 introduced by linear interpolation procedure, summary statistics of actual atmospheric readings
213 and actual readings + imputed CO₂ values were compared statistically. This approach enabled us
214 to take advantage of >25,000 time points throughout the 3 yr period of observation, providing
215 hourly resolution. Mean $p\text{CO}_{2\text{air}} = 437 \pm 20.0 \mu\text{atm}$ (Table 1), variability that falls well within
216 manufacturer's specifications (see section 2.2.4).

217

218 2.2.3 CO₂ gradient (ΔC)

219 ΔC was determined by subtraction, $p\text{CO}_{2\text{water}} - p\text{CO}_{2\text{air}}$, where positive ΔC values correspond to
220 higher CO₂ concentrations in the water, tending toward movement from water to air (outgassing
221 or evasion, where Rhode River = CO₂ source), and negative values that signal CO₂ transport
222 from air to water (dissolution, where Rhode River = CO₂ sink). Figure 2 shows $p\text{CO}_{2\text{water}}$ and
223 $p\text{CO}_{2\text{air}}$ plotted on an hourly basis for the 3 yr period beginning 01 July 2018 and ending 01 July
224 2021. Across this period, ΔC was predominantly negative during cold months and predominantly
225 positive during warm months when $p\text{CO}_{2\text{water}}$ tended to reach the highest values of the year, but
226 ΔC sometimes reversed sign due to occasional extreme day-time photosynthetic drawdown of
227 CO₂ (Fig. 2).

228

229 2.2.4 Accuracy of CO₂ measurements

230 Estimated accuracy of the spherical falling film equilibrator and NDIR sensor (SenseAir K30,
231 <https://senseair.com/>) combination were experimentally determined in the lab and found to
232 measure water equilibrated with known gas concentrations to be within the $\pm 1\%$ uncertainty
233 limits of the of certified standard gas mixtures used, and well within the published accuracy
234 specification of the SenseAir K30 (i.e., $\pm 30 \text{ ppmv} \pm 3\%$ of instrument reading). Experimental
235 analysis by Martin et al. (2017) report even higher accuracy when relative humidity and
236 atmospheric pressure are controlled for. Details on performance of the spherical falling film
237 equilibrator, such as accuracy, precision, and time constants can be found in Miller et al. (2019).
238 Although SenseAir offers automated calibration via long term comparisons to atmospheric
239 readings, this feature was deactivated. The K30 NDIR was periodically validated using standard
240 zero CO₂ (nitrogen) and standard certified span gases at intervals of one to two months during
241 the study period. Although the K30 was never observed to drift beyond its factory specifications,

242 the sensor was occasionally re-calibrated in the lab, and measured values were accepted without
243 adjustment.

244

245 CO₂ measurements were downloaded to a database at approximately two-week intervals during
246 the observation period. Data were graphed and reviewed visually, in combination with twice
247 weekly observations of equilibrator function recorded in an accompanying notebook. Anomalous
248 data were flagged and excluded from data analysis (e.g., flooding or clogging events that
249 interrupted proper equilibration.)

250

251 2.3 Co-located water quality and atmospheric measurements

252 This water quality station at the SERC dock is a long-term node of the Maryland Department of
253 Natural Resources “Eyes on the Bay” Chesapeake Bay tidal water monitoring program, and has
254 been operated by the SERC since 1986. Water quality and atmospheric data are maintained by
255 the MarineGEO Upper Chesapeake Bay Observatory and can be accessed online (Benson et al.,
256 2023). A YSI EXO2 sonde was positioned 1 m below the water’s surface and in proximity (~2.5
257 m distance) to the submerged water pump that fed the *p*CO₂ equilibrator. Sonde measurements
258 were made at 6 minute intervals and aggregated to 1 hr averages. The published accuracy
259 specifications for the YSI sonde are as follows: temperature: ±0.01 °C (-5° to 35° C); salinity:
260 ±1% of reading or 0.1 ppt (0–70 ppt); dissolved oxygen: ±0.1 mg/L or 1% of reading (0 to 20
261 mg/L). Discrete measurements of temperature and salinity were made with a handheld YSI
262 Professional Plus 2030 with Quattro Cable instrument, with the following specifications:
263 temperature: ±0.02 °C (-5° to 70° C); salinity: ±1% of reading or 0.1 ppt (0–70 ppt); dissolved
264 oxygen: ±0.2 mg/L or 2% of reading (0 to 20 mg/L). Equilibrator temperature was measured
265 with a probe (EDS model OW-TEMP-B3-12xA) accurate to ±0.5 °C (-10° to 85 °C). Discrete
266 measurements were routinely compared with the sonde to corroborate measurement agreement.
267 Wind speed measurements were made using a sonic anemometer (Vaisala WXT-520 weather
268 transmitter) mounted 7 m above the mean low tide height of the water and located directly above
269 the *p*CO₂ equilibrator.

270

271 2.4 Data Processing

272 Data included in this study span 01 Jul 2018 to 01 Jul 2021.

273 2.4.1 Gas-specific solubility

274 To determine the purely physical effects of temperature and salinity on CO₂ solubility, gas-
 275 specific solubility values K_0 (mmol · m⁻³ · μatm⁻¹) were calculated across the 3 yr observation
 276 period using water temperature and salinity measurements in combination with $p\text{CO}_{2\text{water}}$ values,
 277 according to Weiss and Price (1980) at 1 hour intervals.

278

279 2.4.2 Gas transfer velocity estimation (k)

280 Given the similarities between the Rhode River and New River estuaries (e.g., shallow,
 281 microtidal estuaries with slow water velocity and strong diel cycles in $p\text{CO}_2$ and DO), we chose
 282 to parameterize gas transfer velocity k (cm · h⁻¹) standardized to the unitless Schmidt number
 283 600 (k_{600}) according to the estuary-specific k parameterization model developed by Van Dam et
 284 al. (2019). Van Dam et al. (2019) determined that k correlated with wind speed differently during
 285 daytime versus nighttime hours (linear vs. parabolic relationships). Wind speed data were
 286 collected during the 3 yr period from a sonic anemometer located on the SERC dock directly
 287 above the equilibration system and approximately 7 m above the water's surface at mean low
 288 tide height. For the analysis, windspeeds were standardized for a height of 10 m following a
 289 power-law relationship, $U_{10} = U_7 * (10/7)^{0.15}$ (Saucier, 2003). Following Van Dam et al.,
 290 wind speed data were binned to 1.5 m s⁻¹ intervals for day and night readings and raw values
 291 replaced by the mean wind speed for each bin. The median binned windspeed over the Rhode
 292 River was 2.2 m s⁻¹, regardless of time of day or season. Recorded windspeeds never exceeded
 293 10m s⁻¹ and were dominated by much lower values (Fig. S1). Unlike the New River Estuary, the
 294 Rhode River's windspeed profile does not differ much between day and night, nor across season.
 295 For this reason, we chose to use the most conservative k_{600} formulation from Van Dam et al
 296 (2019), that combines day and night winds to estimate k_{600} .

297

298 Wind speed was used to parameterize k_{600} as follows:

299

$$300 \quad k_{600} = 1.5 * U_{10} + 4.2 \quad (2)$$

301

302 where U_{10} = mean of binned wind speed at 10 m above the water's surface (m · s⁻¹).

303

304 2.4.3 CO₂ flux

305 Using continuous, parallel 3 yr records (01 July 2018 to 01 July 2021) of dissolved and
 306 atmospheric *p*CO₂, water temperature, salinity, and wind speed (at standard 10m height, *U*₁₀),
 307 CO₂ flux was derived according to the equation:

$$309 \quad \text{CO}_2 \text{ flux} = k_{600} \cdot K_0 \cdot \Delta C \cdot (600 / Sc)^{-0.5} \quad (3)$$

310 where

311 CO₂ flux = the rate and direction of CO₂ mass moving between water and gas phases
 312 (mmol · m⁻² · hr⁻¹)

313 *k*₆₀₀ = gas transfer velocity (cm · hr⁻¹), normalized to a common Schmidt number
 314 (*Sc* = 600)

315 *K*₀ = gas-specific solubility for CO₂ (mmol · m⁻³ · μatm⁻¹)

316 Δ*C* = air-water concentration gradient (μatm)

317 *Sc* = Schmidt number

318

319 Note: CO₂ flux calculations require conversion from traditional *k*₆₀₀ units (cm · hr⁻¹) to (m · hr⁻¹)
 320 from Δ*C* units (μatm) to (atm) prior to calculation.

321

322 2.4.4 Day/Night Designation

323 To differentiate daytime from nighttime hours, we used the position of the measurements
 324 (latitude) in the Rhode River, combined with the local date and time. This approach enabled us to
 325 uniformly designate various environmental measurements as happening during the day or night
 326 (R package "LakeMetabolizer", Winslow et al., 2016).

327

328 2.4.5 Seasonality

329 We chose to break the year into two 6 month periods based seasonal water temperature shifts,
 330 designating June–November as “warm-water months” when water temperatures averaged 23.2 ±
 331 6.90 °C. (mean ± 1 sd) and December–May as “cold-water months”, 10.9 ± 5.66 °C (Figs. S1 and
 332 S2).

333

334

335 2.4.6 Effect size

336 Owing to the large number of observations available for comparison in this study, the likelihood
337 of finding statistically significant results is quite high. Whether such statistical results by
338 themselves connote practical and informative differences can be difficult to discern. Effect sizes
339 (Omega-squared, ω^2) were calculated according to two-factor ANOVAs where independent
340 variables were investigated by season (cold-water vs. warm-water season), day/night period and
341 the interaction of season and day/night. The independent variables compared were: K_0 , CO₂ flux,
342 $\Delta p\text{CO}_2$, k_{600} , $p\text{CO}_{2\text{air}}$, $p\text{CO}_{2\text{water}}$, and wind speed. To account for temporal autocorrelation and
343 lack of independence of observations that are typical of environmental time series data, we
344 corrected for overinflation in the residual mean square used in the effect size calculations by
345 removing the autocorrelation present within residuals, leaving the white-noise component as the
346 unbiased estimate of residual variability (Cochrane-Orcutt procedure, R package "orcutt", Spada
347 et al., 2018).

348

349 **3. Results and Discussion**

350 3.1 Daily and Seasonal Cycling of $p\text{CO}_2$

351 Hourly averaged measurements of $p\text{CO}_{2\text{water}}$ in the Rhode River across three years revealed
352 strong diel and seasonal cycling (Fig. 2). Mean and maximum $p\text{CO}_{2\text{water}}$ were significantly higher
353 in warm-water vs. cold-water months (Table 1). During warm-water months (Jun–Nov) daily
354 oscillations of $p\text{CO}_2$ frequently transit from far above to below ambient atmospheric conditions
355 over the course of the day, only to reverse direction (from low to high) during the nighttime
356 hours (Fig. 2). During the summer, $p\text{CO}_{2\text{water}}$ levels sometimes shifted by as much as 4500 μatm
357 in both directions during a single 24 hr period (Fig. 2). This pattern is consistent with
358 biologically driven cycling whereby very high early morning $p\text{CO}_{2\text{water}}$ conditions are depleted
359 by net photosynthetic activity (inorganic carbon fixation) over the course of the day, but high
360 $p\text{CO}_{2\text{water}}$ is restored by respiration in the benthos and water column at night (Song et al. 2023).
361 Comparing dissolved oxygen (DO) over the same period, similar harmonic cycling is observed,
362 but maximums and minimums of $p\text{CO}_2$ and DO were inversely related (Fig. S1), hallmarks of a
363 production/respiration driven system (Herrmann et al., 2020; Van Dam et al., 2019).

364

365 **Table 1.** Descriptive statistics comparing seasonality of $p\text{CO}_2$, CO_2 flux and associated
 366 parameters in cold-water (Dec–May) and warm-water seasons (Jun–Nov).
 367

Season	Time Period	Variable	Units	N	Mean	Min	Max	SD
overall	-	CO_2 flux	$\text{mmol} \cdot \text{m}^{-2} \cdot \text{hr}^{-1}$	20971	-0.09	-4.89	11.18	1.823
cold	day	CO_2 flux	$\text{mmol} \cdot \text{m}^{-2} \cdot \text{hr}^{-1}$	4494	-1.39	-4.89	8.26	1.134
cold	night	CO_2 flux	$\text{mmol} \cdot \text{m}^{-2} \cdot \text{hr}^{-1}$	5050	-1.39	-4.66	5.24	0.927
warm	day	CO_2 flux	$\text{mmol} \cdot \text{m}^{-2} \cdot \text{hr}^{-1}$	6007	1.18	-3.95	11.18	1.731
warm	night	CO_2 flux	$\text{mmol} \cdot \text{m}^{-2} \cdot \text{hr}^{-1}$	5421	0.78	-3.97	8.05	1.467
overall	-	K_0	$\text{mmol} \cdot \text{m}^{-3} \cdot \mu\text{atm}^{-1}$	20971	0.04	0.03	0.07	0.011
cold	day	K_0	$\text{mmol} \cdot \text{m}^{-3} \cdot \mu\text{atm}^{-1}$	4494	0.05	0.03	0.07	0.009
cold	night	K_0	$\text{mmol} \cdot \text{m}^{-3} \cdot \mu\text{atm}^{-1}$	5050	0.05	0.03	0.07	0.008
warm	day	K_0	$\text{mmol} \cdot \text{m}^{-3} \cdot \mu\text{atm}^{-1}$	6007	0.03	0.03	0.06	0.007
warm	night	K_0	$\text{mmol} \cdot \text{m}^{-3} \cdot \mu\text{atm}^{-1}$	5421	0.04	0.03	0.07	0.008
overall	-	k_{600}	$\text{cm} \cdot \text{hr}^{-1}$	20971	7.86	5.57	18.36	2.047
cold	day	k_{600}	$\text{cm} \cdot \text{hr}^{-1}$	4494	8.71	5.57	16.33	2.251
cold	night	k_{600}	$\text{cm} \cdot \text{hr}^{-1}$	5050	7.74	5.57	18.36	2.081
warm	day	k_{600}	$\text{cm} \cdot \text{hr}^{-1}$	6007	7.92	5.57	18.36	1.868
warm	night	k_{600}	$\text{cm} \cdot \text{hr}^{-1}$	5421	7.20	5.57	18.36	1.751
overall	-	ΔC	μatm	20971	154	-436	4750	645.8
cold	day	ΔC	μatm	4494	-239	-436	1553	220.9
cold	night	ΔC	μatm	5050	-256	-434	1204	164.2
warm	day	ΔC	μatm	6007	570	-399	4750	745.5
overall	-	$p\text{CO}_{2\text{air}}$	μatm	20971	437	387	500	20.0
cold	day	$p\text{CO}_{2\text{air}}$	μatm	4494	430	390	497	16.0
cold	night	$p\text{CO}_{2\text{air}}$	μatm	5050	432	387	499	17.8
warm	day	$p\text{CO}_{2\text{air}}$	μatm	6007	439	390	499	20.7
warm	night	$p\text{CO}_{2\text{air}}$	μatm	5421	443	387	500	21.5
overall	-	$p\text{CO}_{2\text{water}}$	μatm	20971	591	15	5182	651.8
cold	day	$p\text{CO}_{2\text{water}}$	μatm	4494	191	15	1982	220.9
cold	night	$p\text{CO}_{2\text{water}}$	μatm	5050	176	17	1638	163.9
warm	day	$p\text{CO}_{2\text{water}}$	μatm	6007	1009	47	5182	752.6
warm	night	$p\text{CO}_{2\text{water}}$	μatm	5421	844	38	4855	632.2
overall	-	wind speed	$\text{m} \cdot \text{s}^{-1}$	20971	2.4	0.1	9.8	1.42
cold	day	wind speed	$\text{m} \cdot \text{s}^{-1}$	4494	3.1	0.3	8.9	1.53
cold	night	wind speed	$\text{m} \cdot \text{s}^{-1}$	5050	2.4	0.3	9.1	1.45
warm	day	wind speed	$\text{m} \cdot \text{s}^{-1}$	6007	2.5	0.1	9.8	1.28
warm	night	wind speed	$\text{m} \cdot \text{s}^{-1}$	5421	2.0	0.1	9.1	1.23

368
 369 On the seasonal timescale, $p\text{CO}_2$ was consistently lowest and DO highest during cold-water
 370 months of the year (Dec–May; Fig. S1). Importantly, for both gases the temporal variability (diel

371 cycling; Fig. S2) was most constrained during cold-water months across years, strongly
372 suggesting that carbon fixation exceeds respiration for prolonged periods (weeks to months). In
373 contrast, during warm-water months (Jun–Nov), photosynthesis/carbon fixation and respiration
374 are more evenly balanced, compensating one another over 24 hr periods (i.e., respiration >
375 productivity at night and productivity > respiration during daylight hours; Fig. 2).

376

377 3.2 Air-water concentration gradient = ΔC (μatm)

378 When hourly $p\text{CO}_{2\text{water}}$ and $p\text{CO}_{2\text{air}}$ values (composed of 4 hourly measurements and 20
379 interpolated values per day) were plotted across the three years of observation, the diel and
380 seasonal cycles of $p\text{CO}_{2\text{water}}$ are evident. As expected, atmospheric concentrations of CO_2
381 remained relatively constant compared with aqueous loads. When the mean raw $p\text{CO}_{2\text{air}}$
382 measurements (mean = 435.1, 95% CI [434.4, 435.7]) were compared with raw $p\text{CO}_{2\text{air}}$
383 measurements + imputed estimates (mean = 435.4, 95% CI [435.2, 435.7]) no statistical
384 difference was observed, indicating that no substantial bias was introduced by linear
385 interpolation of atmospheric measurements.

386

387 Although nearshore atmospheric CO_2 concentrations are expected to vary more than those in
388 isolated well-mixed atmosphere (e.g., at the Mona Loa Observatory), annual mean values were
389 consistent and within the published uncertainty of the K30 NDIR sensor, when compared with
390 global measurements conducted at Mona Loa ([Thoning et al., 2023](#)). Local perturbations (e.g.,
391 effects of terrestrial photosynthetic drawdown when wind is absent) were apparent in
392 measurements (Fig. 2) but there were no instances when the measured local atmospheric values
393 were suspiciously high or low for days on end, as compared with expected global mean
394 atmospheric values for the time period (i.e., 408–416 ppmv; <https://www.co2.earth/annual-co2>,
395 [Thoning et al., 2023](#)). This lack of sustained anomalous deviation served as additional
396 confirmation that the K30 was functioning properly and had not drifted outside its calibration
397 range. Importantly, given the extreme diel cycling and seasonal variability of the Rhode River's
398 $p\text{CO}_{2\text{water}}$, the absolute accuracy necessary for determining year-over-year changes in
399 atmospheric or ocean $p\text{CO}_2$ is not a requirement for these CO_2 flux calculations which rely on
400 relative differences between water and atmospheric measurements.

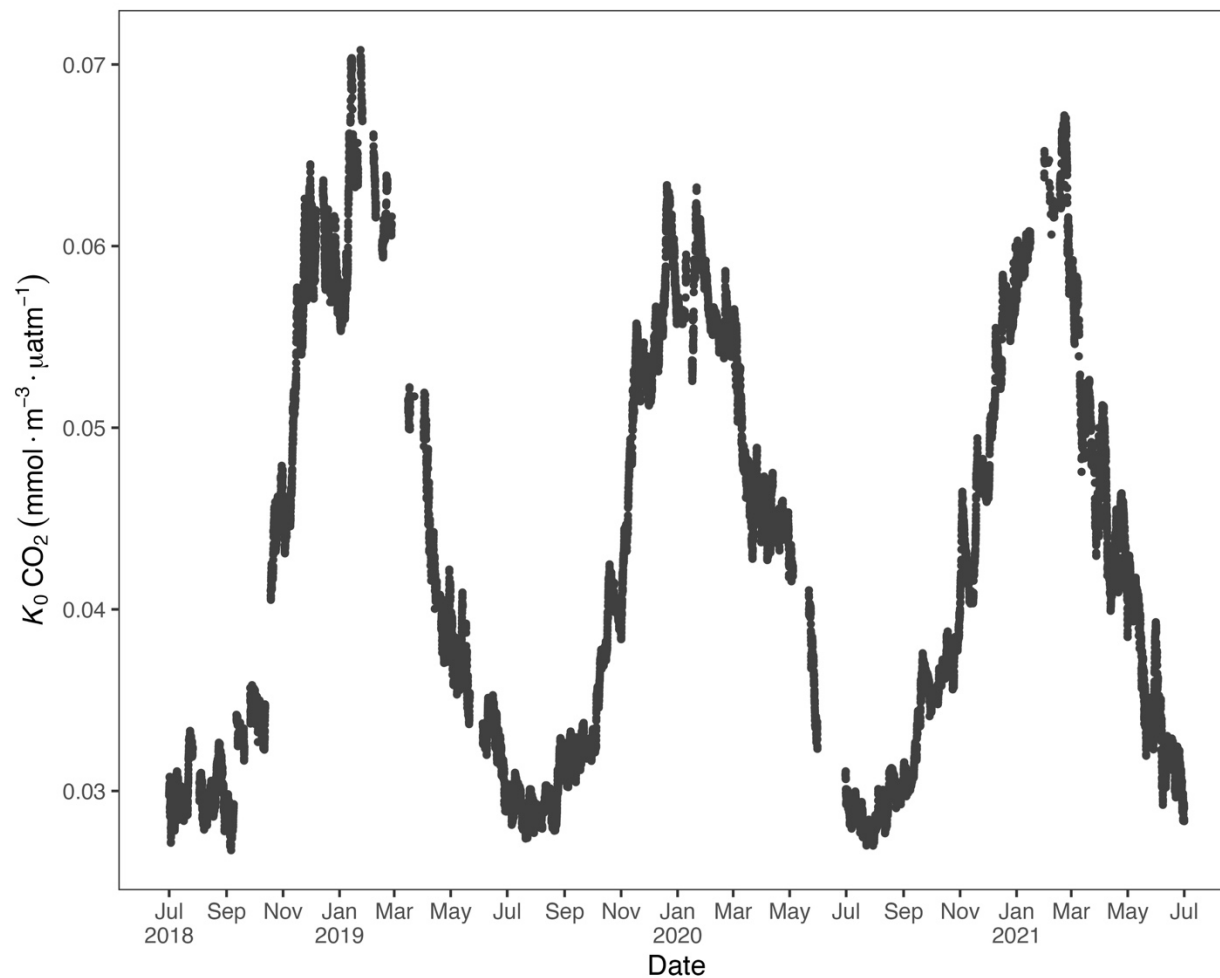
401

402 Hourly air-water concentration gradient values = ΔC (μatm) were calculated and plotted across
403 the three years of study (Fig. 2). During warm months, $p\text{CO}_{2\text{water}}$ routinely shifts from
404 supersaturated to sub-atmospheric and back again, over the course of 24 hours (e.g., between
405 $>2000 \mu\text{atm}$ and $<410 \mu\text{atm}$ on a single day). These large daily swings in $p\text{CO}_{2\text{water}}$ produced
406 concomitant directional reversals of ΔC ($p\text{CO}_{2\text{water}} - p\text{CO}_{2\text{air}}$), which result in longer term
407 averaged gradients (e.g., multi-day, multi-week averages) near zero (Fig. 2). In contrast, most of
408 the time during cold-water months is spent in a state of sub-atmospheric $p\text{CO}_{2\text{water}}$ (under-
409 saturation with respect to overlying atmosphere), resulting in ΔC values that are negative and
410 which promote movement of CO_2 from the atmosphere into the water.

411

412 3.3 Gas-specific solubility (K_0)

413 To account for the physical effects of temperature and salinity on the solubility of CO_2 in
414 estuarine water, K_0 was calculated by methods of Weiss and Price (1980). K_0 varied strongly
415 across seasons over the 3 yr observation period. The maximum annual range = 0.027 to 0.071
416 $\text{mmol} \cdot \text{m}^{-3} \cdot \mu\text{atm}^{-1}$; mean cold-water months = 0.051 and mean warm-water months = 0.035
417 $\text{mmol} \cdot \text{m}^{-3} \cdot \mu\text{atm}^{-1}$, confirming that CO_2 was most soluble during winter and least soluble in
418 summer (Fig. 3). This is inverse to observed dissolved CO_2 values: $p\text{CO}_{2\text{water}}$ was lowest and
419 least variable during winter and highest and most variable during summer (Fig. 2, Table 1)
420 suggesting that solubility, in and of itself, plays only a minor and non-limiting role in $p\text{CO}_{2\text{water}}$
421 in the Rhode River. Effect size (ω^2) estimates indicated that the greatest proportion of variability
422 in K_0 was associated with season, vs. day/night or the interaction of the two (Table 2).



423

424 **Fig. 3.** Gas-specific solubility (K_0) for CO_2 based on water temperature and salinity.

425 Units are $\text{mmol m}^{-3} \mu\text{atm}^{-1}$ in the Rhode River (01 Jul 2018 to 01 Jul 2021).

426 **Table 2.** Contrast effect sizes based on two-factor ANOVA where independent variables were
 427 compared by season (cold-water season = Dec–May vs warm-water season = Jun–Nov),
 428 day/night period and the interaction of the two. ω^2 is a measure of effect size, estimating the
 429 proportion of total variance explained by each parameter. Effect sizes were corrected for inherent
 430 temporal autocorrelation using the Cochran-Orcutt procedure (Spada et al., 2018).
 431

Variable	Factor	Effect Size (ω^2)
K_0	Season	0.0300
K_0	Day/Night	0.000575
K_0	Season:Day/Night	0.0000140
CO ₂ flux	Season	0.415
CO ₂ flux	Day/Night	0.00295
CO ₂ flux	Season:Day/Night	0.00301
ΔC	Season	0.310
ΔC	Day/Night	0.00501
ΔC	Season:Day/Night	0.00333
k_{600}	Season	0.00164
k_{600}	Day/Night	0.00269
k_{600}	Season:Day/Night	0.0000549
pCO_{2air}	Season	0.000137
pCO_{2air}	Day/Night	0.0000134
pCO_{2air}	Season:Day/Night	0.00000137
pCO_{2water}	Season	0.188
pCO_{2water}	Day/Night	0.00275
pCO_{2water}	Season:Day/Night	0.00191
wind speed	Season	0.00711
wind speed	Day/Night	0.0186
wind speed	Season:Day/Night	0.000182

432

433 3.4 Temperature/Biology ratio

434 To independently parse the magnitude of the physical versus biological forcing of pCO_{2water} , we
 435 normalized values to mean water temperature and estimated the Takahashi’s
 436 Temperature/Biology ratio (Takahashi et al., 2002) to compare the influence of temperature and
 437 biological activities on pCO_{2water} . Across the 3-year period, we found that the predominant driver
 438 of pCO_{2water} in the Rhode River was biological activity, accounting for nearly 4 times more
 439 forcing than the physical effects of water temperature on CO₂ solubility (Table 3). These patterns
 440 demonstrate the outsized role that biological processes play in shaping pCO_{2water} in nearshore
 441 marine and estuarine ecosystems (Dai et al., 2022; Van Dam et al., 2019).

442

443

444 **Table 3.** Takahashi Temperature/Biology Ratio (Eq. 5a From Takahashi et al. 2002).
 445

Year	N	$\Delta p\text{CO}_2_{\text{bio}}$	$\Delta p\text{CO}_2_{\text{temp}}$	T/B ratio
2018	4416	3193.0	765.8	0.240
2019	8760	3669.8	1019.6	0.278
2020	8784	2772.1	846.0	0.305
2021	4345	2356.1	507.2	0.215
Overall	26305	3701.5	926.4	0.250

446
447

448 3.5 Gas transfer velocity (k_{600})

449 Gas transfer velocity is affected by both mass transfer from molecular diffusion driven by ΔC
450 (i.e. CO_2 gradient between water and atmosphere) and momentum transfer linked to external
451 environmental forces that enhance turbulence at the air-water boundary layer (Ho et al., 2016;
452 Raymond & Cole, 2001; Van Dam et al., 2019). Van Dam et al. (2019) validated the use of wind
453 speed at 10 m above the water's surface (U_{10}) to estimate gas transfer velocities of CO_2 that were
454 standardized to a Schmidt number of 600 (k_{600}) by comparing estimated values to k_{600} values
455 derived directly from eddy covariance CO_2 flux measurements. Given the relative uniformity of
456 wind speed over the Rhode River where median binned U_{10} windspeed (converted from U_7
457 measurements) was $2.2 \text{ m} \cdot \text{s}^{-1}$ regardless of time of day or season, and that maximum values
458 rarely exceeded $10 \text{ m} \cdot \text{s}^{-1}$ (Table 1, Fig. S1), we chose to use the most conservative estuarine-
459 specific parameterization of k_{600} (Van Dam et al., 2019) (Eq. 2). The mean overall Rhode River
460 k_{600} value for CO_2 (mean \pm SD, $7.86 \pm 2.05 \text{ cm} \cdot \text{hr}^{-1}$) was of comparable magnitude to that of
461 the New River Estuary, NC ($9.37 \pm 9.47 \text{ cm} \cdot \text{hr}^{-1}$). However, wind speed varied far less on the
462 Rhode River than the New River estuary and day/night explained more variability in wind speed
463 than season. Because wind speed directly influenced the formulation of k_{600} (Eq. 2), the effect
464 size of day/night is similarly greater than the seasonal effect on gas transfer velocity (Table 2).
465 Nevertheless, effect sizes (ω^2) indicate that “season” explained at least 10 times more of the
466 observed variance of $p\text{CO}_2_{\text{water}}$, $p\text{CO}_2_{\text{air}}$, air-water concentration gradient, CO_2 flux, and gas-
467 specific solubility than “day/night” or their interaction (Table 2). Given the minor freshwater
468 input and microtidal nature of the Rhode River, we do not believe that lateral water velocity and
469 bottom turbulence appreciably affect the gas transfer velocity of CO_2 here, although we did not
470 investigate possible influences explicitly.

471

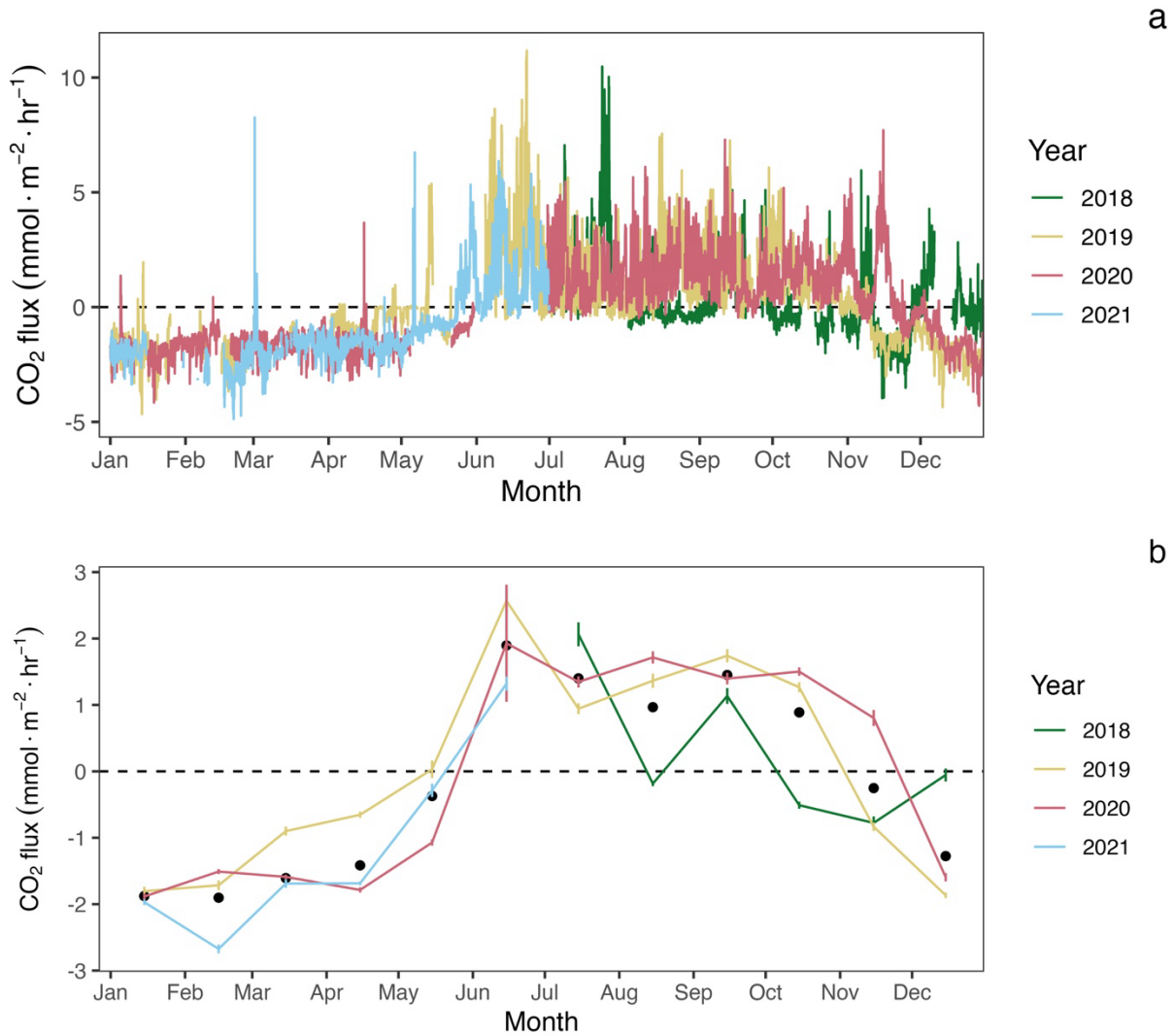
472 Importantly, in coastal marine and estuarine habitats, ΔC can shift as much as several thousand
473 μatm per day due to diel cycling associated with CO_2 production and depletion (Figs. 2, S2). The
474 uncertainty surrounding gas transfer velocity parameterization can represent a major source of
475 error in CO_2 flux calculations (Frankignoulle et al., 1998; Upstill-Goddard, 2006; Wanninkhof &
476 McGillis, 1999); however, small errors in k_{600} have far less effect on CO_2 flux calculations in
477 estuaries which experience $p\text{CO}_2$ swings of several thousand μatm during a single day, compared
478 with more stable conditions of the open ocean where interannual ranges of $p\text{CO}_2$ are typically far
479 less (Van Dam et al., 2019).

480

481 3.6 CO_2 flux - Seasonality and Interannual Variation

482 CO_2 flux was determined according to Eq. 3 using hourly ΔC measurements, CO_2 solubility
483 values (K_0) calculated according to temperature and salinity, and estuary-specific standardized
484 gas transfer velocities (k_{600}) of Van Dam et al. (2019). CO_2 flux was plotted across the three
485 years of observations at hourly and monthly intervals (Fig. 4a-b). As observed with $p\text{CO}_2$, CO_2
486 flux in the Rhode River was shown to be strongly seasonal. Given the similarity in windspeed
487 across seasons (Fig. S1), the effect of differential mean ΔC and variation between warm- and
488 cold-water seasons (Fig. 2, Table 1) almost certainly drives the observed seasonal differences in
489 CO_2 flux (Fig. 4). Again, the specific solubility of CO_2 is greatest at low temperatures, yet this is
490 contrary to the observed mean $p\text{CO}_{2\text{water}}$ patterns, pointing toward a biological mechanism for
491 $p\text{CO}_2$, ΔC , and ultimately, CO_2 flux. The effect size of season on CO_2 flux was two orders of
492 magnitude greater than either day/night or the season day/night by interaction (Table 2).

493



494

495 **Fig. 4.** CO₂ flux estimates by year: a. Hourly, b. Monthly average CO₂ flux estimates with 95%
 496 confidence limits. Black dots in panel b indicate mean monthly fluxes across years.

497

498 Among years, $p\text{CO}_{2\text{water}}$ and CO₂ flux largely repeat themselves, with dissolved CO₂ becoming
 499 consistently sub-atmospheric and CO₂ flux going negative (gas exchange from atmosphere to
 500 water) between December and May and abruptly transitioning to much higher maximum, yet
 501 variable $p\text{CO}_{2\text{water}}$ values with net positive CO₂ fluxes from June through November (Figs. 2 and
 502 4). Monthly averaged CO₂ fluxes are consistent among years (Fig. 4b), with net positive CO₂
 503 fluxes (heterotrophic conditions) between June and November and negative (autotrophic) fluxes
 504 dominating when water temperatures are cold, between December and May. Despite the overall

505 similarities in seasonal CO₂ flux, inter-annual patterns can vary considerably. When hourly CO₂
506 flux values were averaged for the year, the Rhode River in 2019 was shown to have a net
507 positive flux but a net negative flux in 2020. When scaled for the year, 2019 outgassed CO₂ from
508 the water to the atmosphere at a rate of 2215.08 mmol · m⁻² · yr⁻¹ (95% CI = 1816.88, 2613.29).
509 The annual net flux rate in 2020 was negative (i.e. CO₂ moved from the atmosphere into the
510 river) at a rate of -1361.31 mmol · m⁻² · yr⁻¹ (95% CI = -1723.60, -999.01).

511
512 At shorter time scales, such as comparing the same week of the year among years, we sometimes
513 observed vast differences in the magnitude and direction of CO₂ flux (Fig. S3), signaling
514 differences in seasonal conditions between years. Transient events can also result in deviations
515 from otherwise typical CO₂ flux conditions. For example, the period from July 2018 to Jan 2019
516 deviated from other years as CO₂ flux was more erratic, with intermittent periods of negative and
517 positive CO₂ flux extending later into the winter season than in other years. When water
518 temperatures are compared among years, 2018 was shown to be more inconsistent, with more
519 pronounced temperature shifts and reversals than in 2019 or 2020 (Fig. S1). Salinities remained
520 relatively low for the latter half of 2018 into early 2019, reflecting wetter conditions (Fig. S1).
521 There were also two rapid salinity declines (>4 ppt reductions) in July and October 2018, likely
522 associated with strong precipitation events. These events were both followed by immediate
523 spikes in chlorophyll-*a* concentration to levels exceeding 200 μg · L⁻¹, indicative of
524 phytoplankton bloom conditions. From 2018 to 2021, chlorophyll-*a* levels of this magnitude and
525 greater were generally confined to cold-water months (Dec–May; Fig. S1 Erratic water
526 temperature and salinity are also reflected in more variable gas-specific solubility (*K*₀) for CO₂ in
527 2018 than later years (Fig. 3).

528
529 Gallegos et al. (1992) documented predictable phytoplankton blooms associated with freshets in
530 the Rhode River, when nutrient-rich freshwater inundates the estuary, not from point and non-
531 point sources within the local Rhode River watershed, but instead from the enormous watershed
532 that feeds the Susquehanna River, the primary source of freshwater input into the Chesapeake
533 above the Potomac as well as >50% of the entire Bay's freshwater (U.S. Geological Survey,
534 2023). Unlike river dominated estuaries, in the Rhode River estuary, volumetric influxes from
535 the Chesapeake Bay end member far exceed freshwater input from the Muddy Creek and

536 secondary tributaries. In the Rhode River, phytoplankton blooms result in the temporary
537 depletion of $p\text{CO}_{2\text{water}}$, followed by a spike, as phytoplankton senesce and organic carbon is
538 decomposed/re-mineralized back into inorganic carbon. Episodic, short-lived occurrences like
539 these demonstrate how immediate small scale biological forcing, can be coupled with, and
540 catalyzed by, distant large-scale weather and hydrological events. These in turn can influence
541 $p\text{CO}_2$ flux variations within seasons and among years (Fig. 3 and S3; and Chen et al., 2020).

542
543 Overall, except for wind speed, the effect sizes for the other six measured or calculated variables
544 were shown to be greatest for season vs. day/night or the interaction of season x day/night, and in
545 all cases the season effect was greater by at least 1 order of magnitude (Table 2). Seasonality has
546 10 to 1000 times more explanatory power than other variables investigated as estimated by ω^2
547 (Table 2).

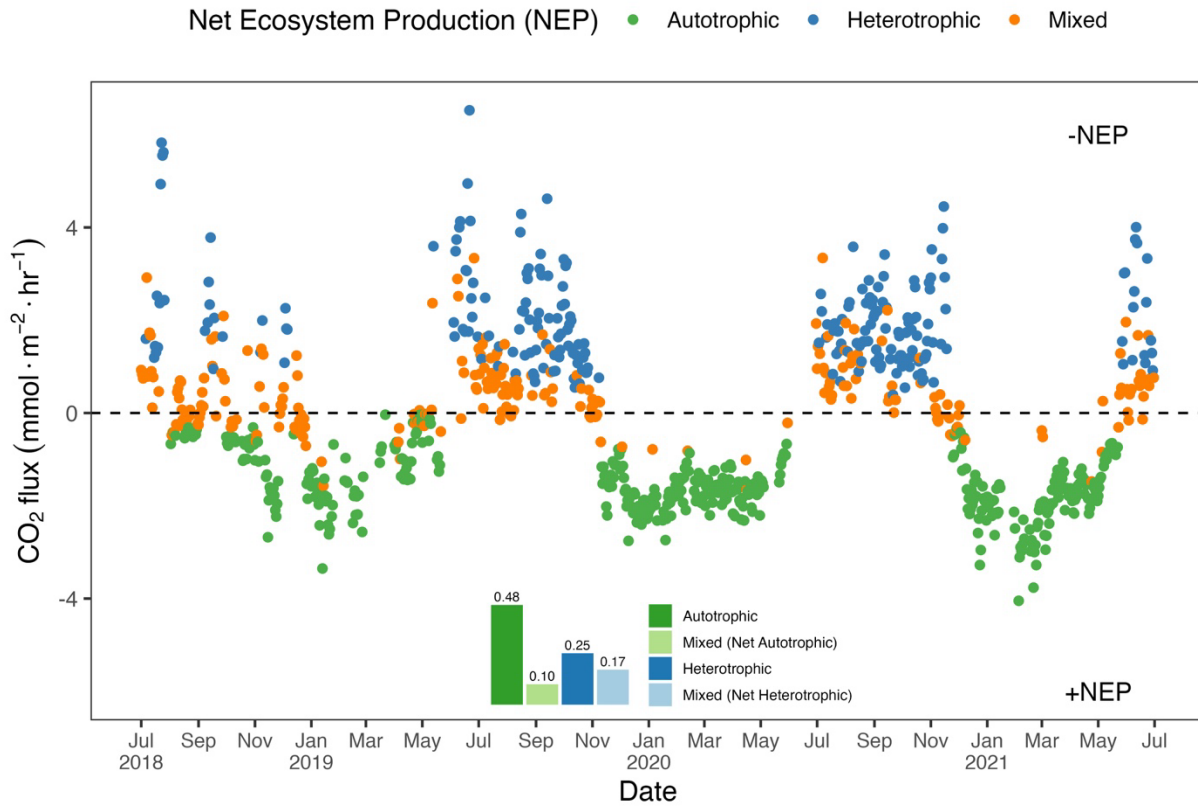
548

549 3.7 Shifting Net Ecosystem Production

550 To better understand how the net ecosystem production (NEP) of the Rhode River shifts
551 throughout the year, where positive NEP indicates the river is storing carbon (autotrophic state)
552 and negative NEP indicates it is releasing carbon to the atmosphere (heterotrophic state), we
553 calculated hourly CO_2 flux values, averaged them by day (i.e. 24 hr period) and plotted each in
554 relation to the $\Delta\text{C} = 0$ reference. Each day of the 3 yr study was categorized as either net
555 heterotrophic (CO_2 flux from water to atmosphere) or net autotrophic (CO_2 flux from atmosphere
556 to water). Each day was then further identified as either purely heterotrophic (all 24 hours were
557 heterotrophic), purely autotrophic, or mixed (some hours were heterotrophic and some were
558 autotrophic but resulting in a net autotrophic or net heterotrophic state for the day) (Fig. 5). From
559 July 2018 to July 2021, most 24 hr periods were categorized as pure autotrophic (444/920 =
560 48%), while 25% (229/990) were purely heterotrophic, and the remainder of mixed trophic status
561 (17% net heterotrophic and 10% net autotrophic; Fig. 5).

562

563



564

565 **Fig. 5.** Daily mean CO₂ flux estimates (CO₂ gradient is CO_{2water} – CO_{2air}). Green dots indicate
 566 days when all 24 hourly flux measurements were negative (autotrophic with +NEP); blue dots
 567 indicate days on which all 24 hourly flux measurements were positive (heterotrophic with -NEP).
 568 Orange dots indicate that hourly fluxes were both negative and positive, and the position of the
 569 orange dot below or above the zero line indicates whether the day was net autotrophic or net
 570 heterotrophic. Insert describes the proportion of days in each category indicating that during 58%
 571 (0.48 + 0.10) of days across three years of observation, the Rhode River was a CO₂ sink.
 572

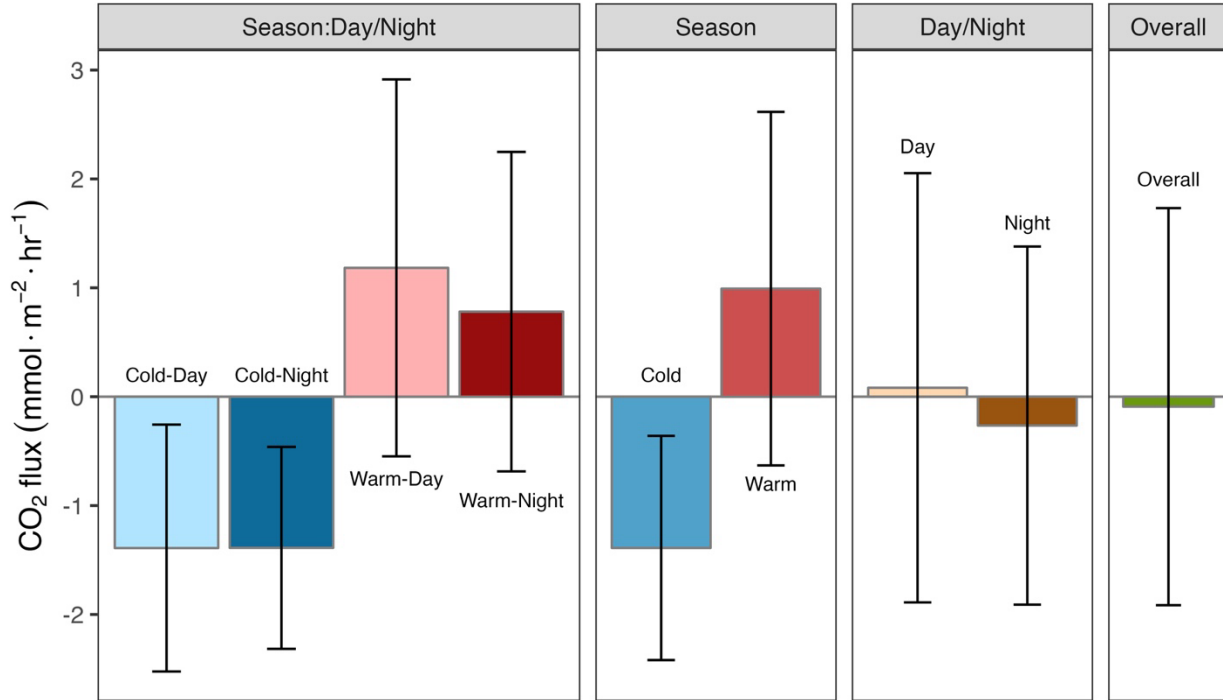
573 Altogether, the Rhode River was net autotrophic for (535 of 920 days = 58%) and net
 574 heterotrophic for 42% (385 days) across three years. When CO₂ flux is integrated over all three
 575 years, the Rhode River is shown to have near neutral NEP (Fig. 6). The effect size of season is
 576 two orders of magnitude greater than either that of day/night or season:day/night interaction
 577 (Table 2). Mean CO₂ flux values highlight the obvious correlation between season and NEP;
 578 error bars (± 1 SD) reveal the importance of diel cycling where the magnitude and directionality
 579 of day/night flux variability is approximately equal to the overall variability accrued across all
 580 three years (Fig. 6). Although CO₂ flux is less variable and more autotrophic during cold-water

581 months than warm-months in the Rhode River, the range of possible values that occur across
582 night and day, regardless of season, must be taken into consideration to minimize incidental
583 sampling bias (Figs. 2 and 6).

584
585 A multi-year investigation of CO₂ flux in the main stem of Chesapeake Bay by Chen et al.
586 (2020) combined several bay-wide cruises that were distributed across seasons to collect discrete
587 and underway *p*CO₂ data for CO₂ flux calculations. They concluded that the low salinity upper
588 bay, which receives large volumes of freshwater from the Susquehanna River, was net
589 heterotrophic; the mesohaline middle bay was net autotrophic, and the polyhaline lower bay was
590 near carbon neutral. Chen et al. (2020) characterized Chesapeake Bay, on the whole, as a weak
591 source of CO₂ to the atmosphere (net flux = 0.73 mol · m⁻² · yr⁻¹) but suggested that during wet
592 years, it may function as weak sink of CO₂. Herrmann et al. (2020) also concluded that the
593 Chesapeake Bay was a weak source of CO₂ to the atmosphere based on calculated *p*CO₂ values
594 from long term pH and alkalinity measurements (net flux = 1.2 mol · m⁻² · yr⁻¹mol). Brodeur and
595 colleagues (2019) examined dissolved inorganic carbon (DIC) and total alkalinity along the
596 mainstem of the Chesapeake Bay across the year in 2016 and concluded that DIC increases from
597 north to south and from surface waters to depth, but that seasonal riverine input and biological
598 cycling were significantly important, concluding that the Bay as a whole was a sink for CO₂.

599
600 When our annual mean *p*CO₂ values were compared with the Chen et al. (2020) survey, the
601 Rhode River was shown to be higher on average and more variable than the mesohaline main
602 stem of the Bay (591 ± 652 vs. 416 ± 167 μatm), including a substantially greater measured
603 range (min = 15, max = 5182 μatm vs. 103 and 1033 μatm). These results suggest that water in
604 the shallow and well mixed Rhode River, and DIC in particular, undergo more acute biological
605 transformation than in the mesohaline main stem of Chesapeake Bay. Chen et al. (2020) point to
606 a variety of factors that affect *p*CO₂ and CO₂ flux in the main stem bay, including temperature,
607 depth, stratification, and freshwater input volume, some of which may attenuate biological
608 forcing. Interannual variability was demonstrated in both the Rhode River (some years were net
609 autotrophic and others heterotrophic, Figs. 4 and 5) and in the mesohaline main stem of the Bay;
610 however, we attribute interannual variability in *p*CO₂ and CO₂ flux primarily to variation in
611 water temperature that in turn drives biological activity. We conclude that seasonal variations the

612 Rhode River (and likely similar rivers in the mesohaline portion of the Chesapeake) are
 613 significant and predictable, closely associated with water temperature, and that temperature
 614 mediates NEP biologically rather than by changes to the solubility of CO₂.



615
 616

617 **Fig. 6.** Mean CO₂ flux \pm 1 SD (mmol · m⁻² · hr⁻¹) plotted by day/night cycling, cold-water/warm-
 618 water season, season by day/night interaction, and overall CO₂ flux across three years of
 619 observation.

620

621 In the Rhode River, we find that CO₂ flux reverses itself daily for part of the year (June–
 622 November) yielding some days that are characterized as a net sink (net autotrophic) and others
 623 that are a net source (net heterotrophic). From December to May, diel cycling is minimal and the
 624 river is almost exclusively a net sink, autotrophic both day and night. Finally, although CO₂ flux
 625 is pronounced but variable across seasons, the net CO₂ flux of the Rhode River on an annual
 626 basis is near neutral.

627

628

629

630

631 3.8 Lateral transport

632 Tidal cycling has been shown to liberate and laterally transport DOC from brackish marshes to
633 adjacent estuaries (Cai, 2011; Herrmann, 2015) and therefore is of great importance to carbon
634 cycling and budgets of wetlands and estuaries (Najjar et al., 2020). DOC outwelling from the
635 Kirkpatrick Marsh (hereafter KPM), a 0.21 km² tidal marsh located approximately 1 km up
636 estuary from our primary study site at the SERC Dock (Fig. 1), into the Rhode River has been
637 measured and modeled extensively in recent years (Clark et al., 2020; Menendez et al., 2022;
638 Tzortziou et al., 2011; Tzortziou et al., 2008). These studies indicate that the KPM is responsible
639 for a large portion of overall DOC input to the Rhode River, as well as significant export from
640 the river to the mainstem of Chesapeake Bay. Model generation and validation by Clark et al.
641 (2020) indicate that up to 13.1% of the total DOC input to the Rhode River originates in the
642 KPM. Another important source (53% of total) is DOC derived from phytoplankton and is
643 therefore labile and readily biodegraded and remineralized into DIC. Furthermore, large
644 quantities of other, semi-labile forms of DOC are exported from the KPM, which are themselves
645 subject to photochemical and biodegradation and remineralization (Clark et al., 2020).
646 Importantly, each of these DOC streams provides a potential source of DIC, including $p\text{CO}_2$, to
647 the Rhode River.

648
649 Dissolved inorganic carbon generated in brackish tidal wetlands is also outwelled directly into
650 estuaries (e.g., Cai et al., 2000; Chu et al., 2018; Song et al., 2023). Recent work by Song et al.
651 (2023) demonstrates that $p\text{CO}_2$ in a salt marsh tidal creek in Waquoit Bay, MA was regulated by
652 both tide height (inversely) and the day/night cycle, with nighttime low tides resulting in the
653 highest $p\text{CO}_2$ values, signaling a strong local effect from respiration and photosynthesis in
654 combination with tidal outwelling.

655
656 In the Rhode River watershed $p\text{CO}_2$ was measured continuously in the single tidal creek that
657 drains the KPM using the same methods as at our primary study location. We observed that the
658 KPM tidal creek $p\text{CO}_2$ follows the tidal cycle exclusively, yet outside the mouth of the tidal
659 creek, in the estuary proper, day/night cycling overwhelms this marsh tidal signal. Simultaneous
660 $p\text{CO}_2$ measurements from the SERC dock follow a strict day/night cycle (Fig. S4). However,
661 while peak levels of dissolved CO_2 in the Kirkpatrick Marsh creek occur at low tide and can

662 reach values nearly 20 times greater than highs at the SERC dock (Fig. S4) there is no obvious
663 evidence of this tidal DIC input at the dock site. Remineralization of DOC exported from the
664 KPM, as well as DOC originating in other locations within the watershed are important sources
665 of DIC in the river, but given the relative volumes of these sources to that of the much larger
666 estuary, as well as the physical distance (~1 km) from SERC dock, these input signals should be
667 expected to be lagged and damped inside the estuary and not tightly coupled with tidal cycles.
668 Instead, $p\text{CO}_2$ exported from the KPM is expected to undergo significant dilution effects, be
669 partially off-gassed to the atmosphere, and be metabolized via photosynthesis, reducing its
670 influence on downstream sites. These findings suggest that despite periodic extreme $p\text{CO}_2$ in
671 KPM tidal creek (>30,000 ppmv), the overall mass of CO_2 export is not sufficient to have
672 measurable effects on the deeper, well-mixed portions of the Rhode River.

673
674 Thus, although land – sea interfaces and outwelling of DOC and DIC are important in estuaries
675 and coastal ecosystems, the relative sizes of wetlands and adjacent water bodies and the overall
676 volume of water moving between the two are also important factors. In eutrophic estuaries like
677 the Rhode River, biological forcing can rapidly assimilate DIC and degrade and mineralize labile
678 forms of DOC, as evidenced by extensive diel cycling in these systems (e.g., Brodeur et al. 2019;
679 Song et al. 2023, and the present study.) The much larger and complex Chesapeake Bay
680 generally follows seasonal changes in $p\text{CO}_2$ and CO_2 flux, but these appear to be most
681 predictable in the upper oligohaline portion and the polyhaline region of the bay near the mouth,
682 where freshwater and oceanic end-member effects are most pronounced (Brodeur et al. 2019;
683 Chen et al., 2020). The central mesohaline part of Chesapeake Bay comprises numerous discrete
684 and unique watersheds and subestuaries/ivers, each of which exchanges water with the bay.
685 Elucidating spatial and temporal patterns of $p\text{CO}_2$ and CO_2 flux are vital for understanding each
686 one's role as an atmospheric source or sink, but also could provide better insight into how each
687 may be influenced by global increases in atmospheric CO_2 (i.e., acidification and its influences
688 on estuarine metabolism, and the local biota, fisheries, and habitats each support.) Collectively,
689 these and other subestuaries will have cumulative effects on the overall water quality of
690 Chesapeake Bay, including cycling of DOC and DIC, which in turn affect $p\text{CO}_2$ and CO_2 flux.

691
692

693 4. Conclusion

694 The notion that estuaries are predominantly heterotrophic systems that invariably outgas more
695 CO₂ to the atmosphere than they absorb has been a long-held view (Abril et al., 2000; Borges et
696 al., 2004; Cai, 2011; Cai et al., 2000; Chen, 2013; Frankignoulle et al., 1998, Gattuso et al.,
697 1998). However, more recently investigators have realized that physical and hydrological
698 characteristics, geographical location, size, and biological and biogeochemical activities may
699 individually, or together, influence CO₂ flux in estuaries and therefore contributions to
700 atmospheric chemistry (Brodeur et al. 2019; Caffrey, 2004; Chen et al., 2013, 2020; Herrmann et
701 al., 2020). As indicated in this study and others, the role that biological processes play in
702 estuaries to either fix CO₂ (autotrophy) or liberate CO₂ (heterotrophy) are extensive, complex,
703 and can be quite variable over space and time (Brodeur et al. 2019; Chen et al., 2020; Herrmann
704 et al., 2020; Rosentreter et al., 2021). High frequency automated measurements revealed strong
705 seasonal contrasts in dissolved CO₂ content and CO₂ flux between water and atmosphere of the
706 Rhode River, a shallow mesohaline reach of the Chesapeake Bay. Importantly, only through high
707 frequency, multi-year measurements could diel and seasonal cycling be fully discerned. Indeed,
708 inadequate sampling can induce bias (e.g., upscaling from a small number of daytime samples
709 taken during warm-water months can skew apparent patterns; Laruelle et al., 2017; Van Dam et
710 al., 2019.). The timing and frequency of measurements are critical and have potential for strong
711 and misleading biases if sampling is insufficient. In contrast, cold-water months coincide with
712 long periods (weeks to months) of continuous sub-atmospheric sink conditions for CO₂. Using
713 these measurements, we estimated the direction and magnitude of CO₂ flux in hourly, daily, and
714 annual terms. In the Rhode River CO₂ flux reverses itself daily for part of the year (June through
715 November) yielding some days that are characterized as net sink (net autotrophic and NEP > 0)
716 and others that are net source (net heterotrophic and NEP < 0). From December to May diel
717 cycling is minimal, and the river is almost exclusively a CO₂ sink with +NEP both day and night.
718 Although CO₂ flux is pronounced but variable across seasons, the net CO₂ flux of the Rhode
719 River on an annual basis is near carbon neutral, although some years are net heterotrophic and
720 others net autotrophic.

721

722 High frequency sampling of *p*CO₂, although typically confined spatially, is one approach to
723 understanding fundamental aspects of estuarine metabolic states and CO₂ flux that may

724 otherwise go undetected (Song et al., 2023). To address the spatial complexity of estuarine,
725 nearshore, and inland waters, more observation locations are required. As with any
726 environmental or ecological question, careful sampling design is critical to balance efficiency
727 and statistical power.

728

729 As the largest and arguably most complex estuary in the United States, the Chesapeake Bay is
730 the subject of extensive ecosystem management efforts and ranks among the most studied and
731 monitored estuaries in the world (Boesch and Goldman 2009). Yet, information on CO₂ and
732 GHG fluxes continue to be limited (Brodeur 2019; Chen et al., 2020; Herrmann et al., 2020).
733 Given the extensive coordinated monitoring programs that either make real-time water quality
734 measurements and/or maintain routine water sampling schedules (e.g., Maryland DNR “Eyes on
735 the Bay” program) in this region, existing water quality observation assets and sampling
736 programs could be leveraged to more fully characterize and quantify CO₂ and other GHG
737 dynamics and flux in the Bay and elsewhere (see Saba et al. 2019). For example, coordinated
738 deployment of additional automated sampling devices (e.g., robust air-water equilibrators and
739 traditional atmospheric gas sensors) in key locations would enable estimates of CO₂ flux, and if
740 combined with pH, DIC, or total alkalinity measurements, carbonate chemistry calculations as
741 well. Importantly, such installations need not be permanent. Instead, a small group of
742 instruments could be systematically deployed across an existing observation network, co-located
743 with other water quality instruments using a stratified sampling approach to capture spatial
744 variability. For example, a set of shifting two to four week deployments during summer and
745 winter months could yield sufficient data to advance our understanding of Chesapeake Bay-wide
746 CO₂ flux significantly in a single year. Such information would complement underway transects
747 that are vital, but which tend to underestimate temporal variability in any given location. In the
748 case of dissolved GHGs, liquid-air equilibration techniques are being used to measure multiple
749 GHGs (Call et al. 2015; Hartmann 2018; Gülzow et al. 2011; Miller et al. 2019; Xiao et al.
750 2020).

751

752 Understanding the GHG dynamics in estuaries is a vital component to generating accurate global
753 budgets (Maher & Eyre, 2012) as well as informing where emerging carbon capture
754 technologies, including nature-based solutions, might be best located (Bradshaw & Dance, 2005;

755 Sun et al., 2021). In the case of estuaries, there have been extensive global losses of seagrasses
756 due to habitat degradation, pollution, and disease (Waycott et al. 2009). In addition to many
757 other ecosystem service benefits, restoration of seagrass and submerged aquatic vegetation has
758 the potential to restore and enhance natural carbon sequestration (i.e. blue carbon; Kennedy et al.
759 2022; Macreadie et al. 2022; Unsworth et al. 2022). In Virginia, U.S.A., Oreska et al. (2020)
760 demonstrated how the functional benefits of a restored seagrass meadow habitat can be
761 quantified ecologically in terms of their ability to sequester carbon and affect GHG fluxes
762 between the estuary and atmosphere. Uniquely, these investigators then monetized the costs and
763 benefits of habitat restoration and function as CO₂ offset credits, as part of a GHG budget, and
764 demonstrated how such approaches can be used to incentivize habitat restoration (Oreska et al.
765 (2020).

766

767 Increasing the completeness and utility of global GHG budgets, as they relate to human activities
768 and ecosystem functions, are necessary steps toward combating global climate change.

769 Measurement of GHGs at high spatial and temporal resolution using economical, automated
770 measurement solutions can increase our understanding of GHG dynamics at small ecologically
771 significant scales, as well as at the larger ecosystem level of an estuary.

772

773 **Data Availability**

774 Hourly means of *p*CO₂ and associated environmental data used in the analyses are available at
775 the Smithsonian Figshare repository <https://doi.org/10.25573/serc.22491655> via under Creative
776 Commons license [CC BY-NC 4.0](https://creativecommons.org/licenses/by-nc/4.0/).

777

778 **Author Contributions**

779 AWM contributed to project Conceptualization, Funding acquisition, Investigation,
780 Methodology, Project Administration, Resources, Supervision and Writing – Original Draft.
781 JRM contributed to Data Curation, Formal Analysis, Software and Visualization. ACR
782 contributed to Data Curation, Investigation, Methodology and Project Administration. MSM
783 contributed to Conceptualization, Supervision and Visualization. KJK contributed to
784 Conceptualization, Data Curation, Software, Validation. All authors contributed to Writing –
785 review and editing.

786

787 **Competing Interests**

788 The corresponding author has declared that none of the authors has any competing interests.

789

790 **Acknowledgments**

791 We thank Patrick Neale and Stephanie Wilson for their early review and critical feedback on this
792 manuscript, as well as J. Patrick Megonigal for discussions on methodology and two anonymous
793 reviewers who contributed beneficial suggestions. Funding for this research was provided by the
794 Smithsonian Institution.

795

796 **References**

797 Abril, G. and Borges, A. V.: Carbon Dioxide and Methane Emissions from Estuaries, in:
798 Greenhouse Gas Emissions — Fluxes and Processes: Hydroelectric Reservoirs and Natural
799 Environments, edited by: Tremblay, A., Varfalvy, L., Roehm, C., and Garneau, M., Springer,
800 Berlin, Heidelberg, 187–207, https://doi.org/10.1007/978-3-540-26643-3_8, 2005.

801 Abril, G., Etcheber, H., Borges, A. V., and Frankignoulle, M.: Excess atmospheric carbon
802 dioxide transported by rivers into the Scheldt estuary, *Comptes Rendus de l'Académie des*
803 *Sciences - Series IIA - Earth and Planetary Science*, 330, 761–768,
804 [https://doi.org/10.1016/S1251-8050\(00\)00231-7](https://doi.org/10.1016/S1251-8050(00)00231-7), 2000.

805 Bauer, J. E., Cai, W.-J., Raymond, P. A., Bianchi, T. S., Hopkinson, C. S., and Regnier, P. A. G.:
806 The changing carbon cycle of the coastal ocean, *Nature*, 504, 61–70,
807 <https://doi.org/10.1038/nature12857>, 2013.

808 Benson, S., Rich, R., Tashjian, A., Lonneman, M., and Neale, P.: MarineGEO Upper
809 Chesapeake Bay Observatory CPOP Data, <https://doi.org/10.25573/SERC.C.6100368.V10>,
810 2023.

811 Boesch, D.F. and Goldman, E.B.: Chesapeake Bay, USA, in: *Ecosystem-Based Management for*
812 *the Oceans*, edited by: McLeod, K. McLeod and Leslie H. Island Press, Washington, D.C., 268–

813 293, 2009.

814

815 Borges, A. V.: Do we have enough pieces of the jigsaw to integrate CO₂ fluxes in the coastal
816 ocean?, *Estuaries*, 28, 3–27, <https://doi.org/10.1007/BF02732750>, 2005.

817 Borges, A. V., Delille, B., Schiettecatte, L.-S., Gazeau, F., Abril, G., and Frankignoulle, M.: Gas
818 transfer velocities of CO₂ in three European estuaries (Randers Fjord, Scheldt, and Thames),
819 *Limnology and Oceanography*, 49, 1630–1641, 2004.

820 Bradshaw, J. and Dance, T.: Mapping geological storage prospectivity of CO₂ for the world's
821 sedimentary basins and regional source to sink matching, in: *Greenhouse Gas Control*
822 *Technologies 7*, vol. I, Elsevier, 583–591, <https://doi.org/10.1016/B978-008044704-9/50059-8>,
823 2005.

824 Breitburg, D. L., Hines, A. H., Jordan, T. E., McCormick, M. K., Weller, D. E., and Whigham,
825 D. F.: Landscape patterns, nutrient discharges, and biota of the Rhode River estuary and its
826 watershed: Contribution of the Smithsonian Environmental Research Center to the Pilot
827 Integrated Ecosystem Assessment, 2008.

828 Brodeur, J. R., Chen, B., Su, J., Xu, Y.-Y., Hussain, N., Scaboo, K. M., Zhang, Y., Testa, J. M.,
829 and Cai, W.-J.: Chesapeake Bay Inorganic Carbon: Spatial Distribution and Seasonal Variability,
830 *Frontiers in Marine Science*, 6, <https://doi.org/10.3389/fmars.2019.00099>, 2019.

831 Broecker, W. S., Takahashi, T., Simpson, H. J., and Peng, T.-H.: Fate of Fossil Fuel Carbon
832 Dioxide and the Global Carbon Budget, *Science*, 206, 409–418, 1979.

833 Caffrey, J. M.: Factors controlling net ecosystem metabolism in US estuaries, *Estuaries*, 27, 90–
834 101, 2004.

835 Cai, W.-J.: Estuarine and Coastal Ocean Carbon Paradox: CO₂ Sinks or Sites of Terrestrial
836 Carbon Incineration?, *Annual Review of Marine Science*, 3, 123–145,
837 <https://doi.org/10.1146/annurev-marine-120709-142723>, 2011.

838 Cai, W.-J. and Wang, Y.: The chemistry, fluxes, and sources of carbon dioxide in the estuarine
839 waters of the Satilla and Altamaha Rivers, Georgia, *Limnology and Oceanography*, 43, 657–668,
840 <https://doi.org/10.4319/lo.1998.43.4.0657>, 1998.

841 Cai, W.-J., Wiebe, W. J., Wang, Y., and Sheldon, J. E.: Intertidal marsh as a source of dissolved
842 inorganic carbon and a sink of nitrate in the Satilla River-estuarine complex in the southeastern
843 U.S., *Limnology and Oceanography*, 45, 1743–1752, <https://doi.org/10.4319/lo.2000.45.8.1743>,
844 2000.

845 Call, M., Maher, D. T., Santos, I. R., Ruiz-Halpern, S., Mangion, P., Sanders, C. J., Erler, D. V.,
846 Oakes, J. M., Rosentreter, J., Murray, R., and Eyre, B. D.: Spatial and temporal variability of
847 carbon dioxide and methane fluxes over semi-diurnal and spring–neap–spring timescales in a
848 mangrove creek, *Geochimica et Cosmochimica Acta*, 150, 211–225,
849 <https://doi.org/10.1016/j.gca.2014.11.023>, 2015.

850 Chen, B., Cai, W.-J., Brodeur, J. R., Hussain, N., Testa, J. M., Ni, W., and Li, Q.: Seasonal and
851 spatial variability in surface pCO₂ and air–water CO₂ flux in the Chesapeake Bay, *Limnology*
852 and *Oceanography*, 65, 3046–3065, <https://doi.org/10.1002/lno.11573>, 2020.

853 Chen, C.-T. A., Huang, T.-H., Chen, Y.-C., Bai, Y., He, X., and Kang, Y.: Air–sea exchanges of
854 CO₂ in the world’s coastal seas, *Biogeosciences*, 10, 6509–6544, [https://doi.org/10.5194/bg-10-](https://doi.org/10.5194/bg-10-6509-2013)
855 [6509-2013](https://doi.org/10.5194/bg-10-6509-2013), 2013.

856 Chu, S. N., Wang, Z. A., Gonneea, M. E., Kroeger, K. D., and Ganju, N. K.: Deciphering the
857 dynamics of inorganic carbon export from intertidal salt marshes using high-frequency
858 measurements, *Marine Chemistry*, 206, 7–18, <https://doi.org/10.1016/j.marchem.2018.08.005>,
859 2018.

860 Clark, J. B., Long, W., Tzortziou, M., Neale, P. J., and Hood, R. R.: Wind-Driven Dissolved
861 Organic Matter Dynamics in a Chesapeake Bay Tidal Marsh-Estuary System, *Estuaries and*
862 *Coasts*, 41, 708–723, <https://doi.org/10.1007/s12237-017-0295-1>, 2018.

863 Clark, J. B., Long, W., and Hood, R. R.: A Comprehensive Estuarine Dissolved Organic Carbon
864 Budget Using an Enhanced Biogeochemical Model, *Journal of Geophysical Research:*
865 *Biogeosciences*, 125, e2019JG005442, <https://doi.org/10.1029/2019JG005442>, 2020.

866 Correll, D. L., Jordan, T. E., and Weller, D. E.: Nutrient flux in a landscape: Effects of coastal
867 land use and terrestrial community mosaic on nutrient transport to coastal waters, *Estuaries*, 15,
868 431–442, <https://doi.org/10.2307/1352388>, 1992.

- 869 Dai, M., Su, J., Zhao, Y., Hofmann, E. E., Cao, Z., Cai, W.-J., Gan, J., Lacroix, F., Laruelle, G.
870 G., Meng, F., Müller, J. D., Regnier, P. A. G., Wang, G., and Wang, Z.: Carbon Fluxes in the
871 Coastal Ocean: Synthesis, Boundary Processes, and Future Trends, *Annual Review of Earth and*
872 *Planetary Sciences*, 50, 593–626, <https://doi.org/10.1146/annurev-earth-032320-090746>, 2022.
- 873 Frankignoulle, M., Abril, G., Borges, A., Bourge, I., Canon, C., Delille, B., Libert, E., and
874 Théate, J.-M.: Carbon Dioxide Emission from European Estuaries, *Science*, 282, 434–436,
875 <https://doi.org/10.1126/science.282.5388.434>, 1998.
- 876 Freeman, L. A., Corbett, D. R., Fitzgerald, A. M., Lemley, D. A., Quigg, A., and Steppe, C. N.:
877 Impacts of urbanization and development on estuarine ecosystems and water quality, *Estuaries*
878 *and Coasts*, 42, 1821–1838, <https://doi.org/10.1007/s12237-019-00597-z>, 2019.
- 879 Freshwater Flow into Chesapeake Bay | U.S. Geological Survey:
880 [https://www.usgs.gov/centers/chesapeake-bay-activities/science/freshwater-flow-chesapeake-](https://www.usgs.gov/centers/chesapeake-bay-activities/science/freshwater-flow-chesapeake-bay)
881 [bay](https://www.usgs.gov/centers/chesapeake-bay-activities/science/freshwater-flow-chesapeake-bay), last access: 21 September 2023.
- 882 Gallegos, C. L., Jordan, T. E., and Correll, D. L.: Event-scale response of phytoplankton to
883 watershed inputs in a subestuary: Timing, magnitude, and location of blooms, *Limnology and*
884 *Oceanography*, 37, 813–828, <https://doi.org/10.4319/lo.1992.37.4.0813>, 1992.
- 885 Gallegos, C. L., Jordan, T. E., and Hedrick, S. S.: Long-term Dynamics of Phytoplankton in the
886 Rhode River, Maryland (USA), *Estuaries and Coasts*, 33, 471–484,
887 <https://doi.org/10.1007/s12237-009-9172-x>, 2010.
- 888 Gattuso, J.-P., Frankignoulle, M., and Wollast, R.: Carbon and Carbonate Metabolism in Coastal
889 Aquatic Ecosystems, *Annual Review of Ecology and Systematics*, 29, 405–434,
890 <https://doi.org/10.1146/annurev.ecolsys.29.1.405>, 1998.
- 891 Gülzow, W., Rehder, G., Schneider, B., Deimling, J. S. v., and Sadkowiak, B.: A new method for
892 continuous measurement of methane and carbon dioxide in surface waters using off-axis
893 integrated cavity output spectroscopy (ICOS): An example from the Baltic Sea, *Limnology and*
894 *Oceanography: Methods*, 9, 176–184, <https://doi.org/10.4319/lom.2011.9.176>, 2011.
- 895 Hartmann, J. F., Gentz, T., Schiller, A., Greule, M., Grossart, H.-P., Ionescu, D., Keppler, F.,
896 Martinez-Cruz, K., Sepulveda-Jauregui, A., and Isenbeck-Schröter, M.: A fast and sensitive

- 897 method for the continuous in situ determination of dissolved methane and its $\delta^{13}\text{C}$ -isotope ratio
898 in surface waters, *Limnology and Oceanography: Methods*, 16, 273–285,
899 <https://doi.org/10.1002/lom3.10244>, 2018.
- 900 Herrmann, M., Najjar, R. G., Kemp, W. M., Alexander, R. B., Boyer, E. W., Cai, W.-J., Griffith,
901 P. C., Kroeger, K. D., McCallister, S. L., and Smith, R. A.: Net ecosystem production and
902 organic carbon balance of U.S. East Coast estuaries: A synthesis approach, *Global*
903 *Biogeochemical Cycles*, 29, 96–111, <https://doi.org/10.1002/2013GB004736>, 2015.
- 904 Herrmann, M., Najjar, R. G., Da, F., Friedman, J. R., Friedrichs, M. A. M., Goldberger, S.,
905 Menendez, A., Shadwick, E. H., Stets, E. G., and St-Laurent, P.: Challenges in Quantifying Air-
906 Water Carbon Dioxide Flux Using Estuarine Water Quality Data: Case Study for Chesapeake
907 Bay, *Journal of Geophysical Research: Oceans*, 125, e2019JC015610,
908 <https://doi.org/10.1029/2019JC015610>, 2020.
- 909 Ho, D. T., Coffineau, N., Hickman, B., Chow, N., Koffman, T., and Schlosser, P.: Influence of
910 current velocity and wind speed on air-water gas exchange in a mangrove estuary, *Geophysical*
911 *Research Letters*, 43, 3813–3821, <https://doi.org/10.1002/2016GL068727>, 2016.
- 912 Jiang, L.-Q., Cai, W.-J., and Wang, Y.: A comparative study of carbon dioxide degassing in
913 river-and marine-dominated estuaries, *Limnology and Oceanography*, 53, 2603–2615, 2008.
- 914 Joesoef, A., Huang, W.-J., Gao, Y., and Cai, W.-J.: Air–water fluxes and sources of carbon
915 dioxide in the Delaware Estuary: spatial and seasonal variability, *Biogeosciences*, 12, 6085–
916 6101, <https://doi.org/10.5194/bg-12-6085-2015>, 2015.
- 917 Jordan, T. E. and Correll, D. L.: Continuous automated sampling of tidal exchanges of nutrients
918 by brackish marshes, *Estuarine, Coastal and Shelf Science*, 32, 527–545,
919 [https://doi.org/10.1016/0272-7714\(91\)90073-K](https://doi.org/10.1016/0272-7714(91)90073-K), 1991.
- 920 Jordan, T. E., Correll, D. L., Peterjohn, W. T., and Weller, D. E.: Nutrient flux in a landscape:
921 The Rhode River watershed and receiving waters, in: *Watershed Research Perspectives*, edited
922 by: Correll, D. L., Smithsonian Institution Press, Washington, DC, 1986.

- 923 Jordan, T. E., Correll, D. L., Miklas, J., and Weller, D. E.: Nutrients and chlorophyll at the
924 interface of a watershed and an estuary, *Limnol. Oceanogr.*, 36, 251–267,
925 <https://doi.org/10.4319/lo.1991.36.2.0251>, 1991.
- 926 Kennedy, H., Pagès, J. F., Lagomasino, D., Arias-Ortiz, A., Colarusso, P., Fourqurean, J. W.,
927 Githaiga, M. N., Howard, J. L., Krause-Jensen, D., Kuwae, T., Lavery, P. S., Macreadie, P. I.,
928 Marbà, N., Masqué, P., Mazarrasa, I., Miyajima, T., Serrano, O., and Duarte, C. M.: Species
929 Traits and Geomorphic Setting as Drivers of Global Soil Carbon Stocks in Seagrass Meadows,
930 *Global Biogeochemical Cycles*, 36, e2022GB007481, <https://doi.org/10.1029/2022GB007481>,
931 2022.
- 932 Klaus, M. and Vachon, D.: Challenges of predicting gas transfer velocity from wind
933 measurements over global lakes, *Aquat Sci*, 82, 53, <https://doi.org/10.1007/s00027-020-00729-9>,
934 2020.
- 935 Lachin, J. M.: Fallacies of last observation carried forward analyses, *Clinical Trials*, 13, 161–
936 168, <https://doi.org/10.1177/1740774515602688>, 2016.
- 937 Laruelle, G. G., Goossens, N., Arndt, S., Cai, W.-J., and Regnier, P.: Air–water CO₂ evasion
938 from US East Coast estuaries, *Biogeosciences*, 14, 2441–2468, [https://doi.org/10.5194/bg-14-
939 2441-2017](https://doi.org/10.5194/bg-14-2441-2017), 2017.
- 940 Macreadie, P. I., Robertson, A. I., Spinks, B., Adams, M. P., Atchison, J. M., Bell-James, J.,
941 Bryan, B. A., Chu, L., Filbee-Dexter, K., Drake, L., Duarte, C. M., Friess, D. A., Gonzalez, F.,
942 Grafton, R. Q., Helmstedt, K. J., Kaebernick, M., Kelleway, J., Kendrick, G. A., Kennedy, H.,
943 Lovelock, C. E., Magonigal, J. P., Maher, D. T., Pidgeon, E., Rogers, A. A., Sturgiss, R.,
944 Trevathan-Tackett, S. M., Wartman, M., Wilson, K. A., and Rogers, K.: Operationalizing
945 marketable blue carbon, *One Earth*, 5, 485–492, <https://doi.org/10.1016/j.oneear.2022.04.005>,
946 2022.
- 947 Maher, D. T. and Eyre, B. D.: Carbon budgets for three autotrophic Australian estuaries:
948 Implications for global estimates of the coastal air-water CO₂ flux, *Global Biogeochemical
949 Cycles*, 26, <https://doi.org/10.1029/2011GB004075>, 2012.

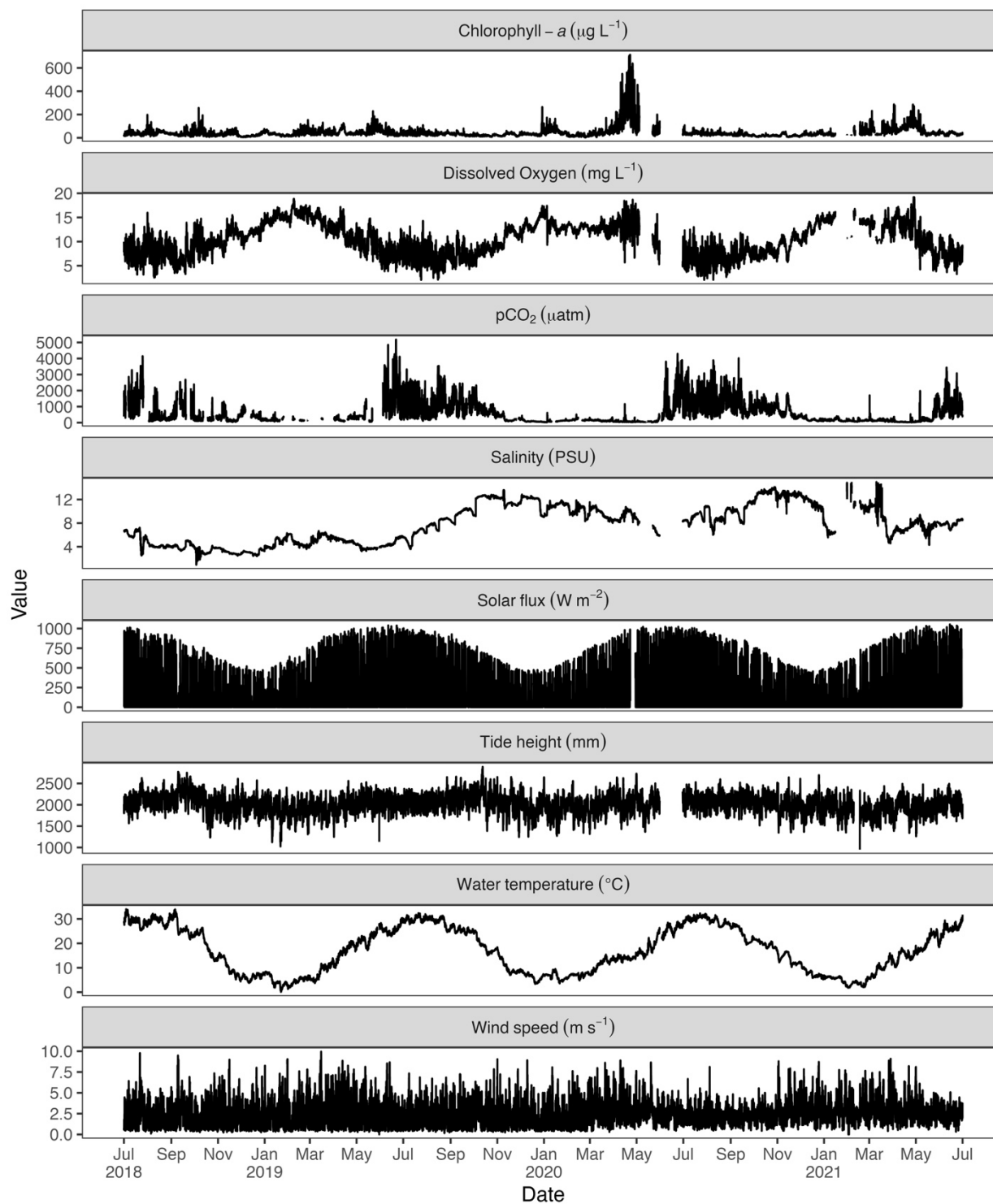
- 950 Martin, C. R., Zeng, N., Karion, A., Dickerson, R. R., Ren, X., Turpie, B. N., and Weber, K. J.:
951 Evaluation and environmental correction of ambient CO₂ measurements from a low-cost NDIR
952 sensor, *Atmospheric Measurement Techniques*, 10, 2383–2395, [https://doi.org/10.5194/amt-10-](https://doi.org/10.5194/amt-10-2383-2017)
953 [2383-2017](https://doi.org/10.5194/amt-10-2383-2017), 2017.
- 954 Menendez, A., Tzortziou, M., Neale, P., Megonigal, P., Powers, L., Schmitt-Kopplin, P., and
955 Gonsior, M.: Strong Dynamics in Tidal Marsh DOC Export in Response to Natural Cycles and
956 Episodic Events From Continuous Monitoring, *Journal of Geophysical Research:*
957 *Biogeosciences*, 127, e2022JG006863, <https://doi.org/10.1029/2022JG006863>, 2022.
- 958 Miller, A. W., Reynolds, A. C., and Minton, M. S.: A spherical falling film gas-liquid
959 equilibrators for rapid and continuous measurements of CO₂ and other trace gases, *PLOS ONE*,
960 14, e0222303, <https://doi.org/10.1371/journal.pone.0222303>, 2019.
- 961 Najjar, R. G., Herrmann, M., Cintrón Del Valle, S. M., Friedman, J. R., Friedrichs, M. A. M.,
962 Harris, L. A., Shadwick, E. H., Stets, E. G., and Woodland, R. J.: Alkalinity in Tidal Tributaries
963 of the Chesapeake Bay, *Journal of Geophysical Research: Oceans*, 125, e2019JC015597,
964 <https://doi.org/10.1029/2019JC015597>, 2020.
- 965 Oreska, M. P. J., McGlathery, K. J., Aoki, L. R., Berger, A. C., Berg, P., and Mullins, L.: The
966 greenhouse gas offset potential from seagrass restoration, *Sci Rep*, 10, 7325,
967 <https://doi.org/10.1038/s41598-020-64094-1>, 2020.
- 968 Raymond, P. A. and Cole, J. J.: Gas Exchange in Rivers and Estuaries: Choosing a Gas Transfer
969 Velocity, *Estuaries*, 24, 312–317, <https://doi.org/10.2307/1352954>, 2001.
- 970 Raymond, P. A., Hartmann, J., Lauerwald, R., Sobek, S., McDonald, C., Hoover, M., Butman,
971 D., Striegl, R., Mayorga, E., Humborg, C., Kortelainen, P., Dürr, H., Meybeck, M., Ciais, P., and
972 Guth, P.: Global carbon dioxide emissions from inland waters, *Nature*, 503, 355–359,
973 <https://doi.org/10.1038/nature12760>, 2013.
- 974 Rose, K. C., Neale, P. J., Tzortziou, M., Gallegos, C. L., and Jordan, T. E.: Patterns of spectral,
975 spatial, and long-term variability in light attenuation in an optically complex sub-estuary,
976 *Limnology and Oceanography*, 64, S257–S272, <https://doi.org/10.1002/lno.11005>, 2019.

- 977 Rosentreter, J. A., Wells, N. S., Ulseth, A. J., and Eyre, B. D.: Divergent Gas Transfer Velocities
978 of CO₂, CH₄, and N₂O Over Spatial and Temporal Gradients in a Subtropical Estuary, *Journal*
979 *of Geophysical Research: Biogeosciences*, 126, e2021JG006270,
980 <https://doi.org/10.1029/2021JG006270>, 2021.
- 981 Saba, G. K., Goldsmith, K. A., Cooley, S. R., Grosse, D., Meseck, S. L., Miller, A. W., Phelan,
982 B., Poach, M., Rheault, R., St.Laurent, K., Testa, J. M., Weis, J. S., and Zimmerman, R.:
983 Recommended priorities for research on ecological impacts of ocean and coastal acidification in
984 the U.S. Mid-Atlantic, *Estuarine, Coastal and Shelf Science*, 225, 106188,
985 <https://doi.org/10.1016/j.ecss.2019.04.022>, 2019.
- 986 Saucier, W. J.: *Principles of Meteorological Analysis*, Dover Publications, 468 pp., 2003.
- 987 Song, S., Wang, Z. A., Kroeger, K. D., Eagle, M., Chu, S. N., and Ge, J.: High-frequency
988 variability of carbon dioxide fluxes in tidal water over a temperate salt marsh, *Limnology and*
989 *Oceanography*, 68, 2108–2125, <https://doi.org/10.1002/lno.12409>, 2023.
- 990 Spada, S., Quartagno, M., Tamburini, M., and Robinson, D.: *orcutt: Estimate Procedure in Case*
991 *of First Order Autocorrelation*, 2018.
- 992 Sun, X., Alcalde, J., Bakhtbidar, M., Elío, J., Vilarrasa, V., Canal, J., Ballesteros, J., Heinemann,
993 N., Haszeldine, S., Cavanagh, A., Vega-Maza, D., Rubiera, F., Martínez-Orio, R., Johnson, G.,
994 Carbonell, R., Marzan, I., Travé, A., and Gomez-Rivas, E.: Hubs and clusters approach to unlock
995 the development of carbon capture and storage – Case study in Spain, *Applied Energy*, 300,
996 117418, <https://doi.org/10.1016/j.apenergy.2021.117418>, 2021.
- 997 Susquehanna River at Conowingo, MD | U.S. Geological Survey:
998 <https://waterdata.usgs.gov/monitoring-location/01578310/>, last access: 28 September 2023.
- 999 Takahashi, T., Sutherland, S. C., Sweeney, C., Poisson, A., Metzl, N., Tilbrook, B., Bates, N.,
1000 Wanninkhof, R., Feely, R. A., Sabine, C., Olafsson, J., and Nojiri, Y.: Global sea–air CO₂ flux
1001 based on climatological surface ocean *p*CO₂, and seasonal biological and temperature effects,
1002 *Deep Sea Research Part II: Topical Studies in Oceanography*, 49, 1601–1622,
1003 [https://doi.org/10.1016/S0967-0645\(02\)00003-6](https://doi.org/10.1016/S0967-0645(02)00003-6), 2002.

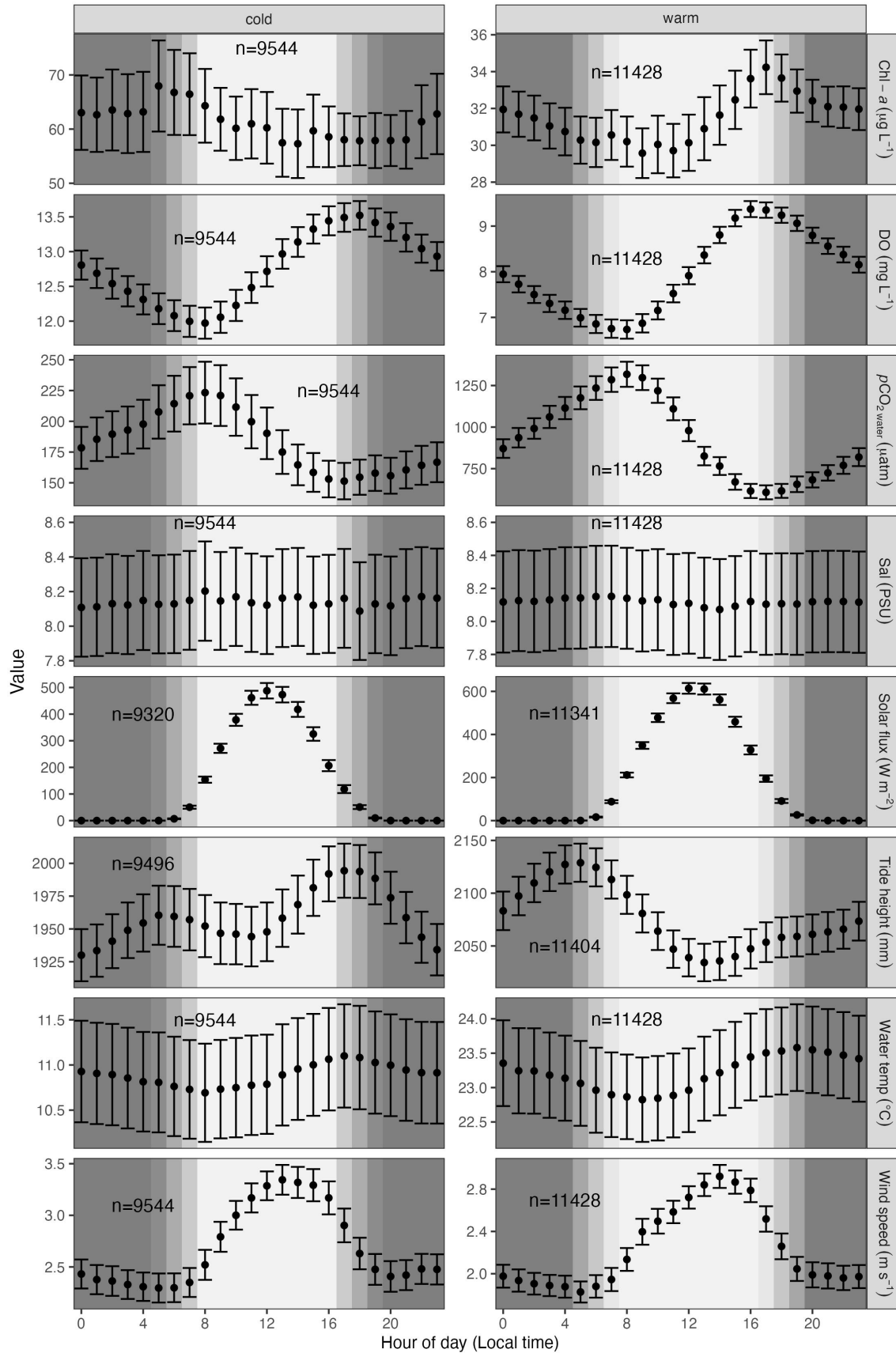
- 1004 Thoning, K. W., Crotwell, A. M., and Mund, J. W.: NOAA Global Monitoring Laboratory
1005 Carbon Cycle and Greenhouse Gases Group Continuous Insitu Measurements of CO₂ at Global
1006 Background Sites, 1973-Present, <https://doi.org/10.15138/YAF1-BK21>, 2023.
- 1007 Tzortziou, M., Neale, P. J., Osburn, C. L., Megonigal, J. P., Maie, N., and Jaff , R.: Tidal
1008 marshes as a source of optically and chemically distinctive colored dissolved organic matter in
1009 the Chesapeake Bay, *Limnology and Oceanography*, 53, 148–159,
1010 <https://doi.org/10.4319/lo.2008.53.1.0148>, 2008.
- 1011 Tzortziou, M., Neale, P. J., Megonigal, J. P., Pow, C. L., and Butterworth, M.: Spatial gradients
1012 in dissolved carbon due to tidal marsh outwelling into a Chesapeake Bay estuary, *Marine
1013 Ecology Progress Series*, 426, 41–56, <https://doi.org/10.3354/meps09017>, 2011.
- 1014 Unsworth, R. K. F., Cullen-Unsworth, L. C., Jones, B. L. H., and Lilley, R. J.: The planetary role
1015 of seagrass conservation, *Science*, 377, 609–613, <https://doi.org/10.1126/science.abq6923>, 2022.
- 1016 Upstill-Goddard, R. C.: Air–sea gas exchange in the coastal zone, *Estuarine, Coastal and Shelf
1017 Science*, 70, 388–404, <https://doi.org/10.1016/j.ecss.2006.05.043>, 2006.
- 1018 Van Dam, B. R., Edson, J. B., and Tobias, C.: Parameterizing Air-Water Gas Exchange in the
1019 Shallow, Microtidal New River Estuary, *Journal of Geophysical Research: Biogeosciences*, 124,
1020 2351–2363, <https://doi.org/10.1029/2018JG004908>, 2019.
- 1021 Wanninkhof, R.: Relationship between wind speed and gas exchange over the ocean, *Journal of
1022 Geophysical Research: Oceans*, 97, 7373–7382, 1992.
- 1023 Wanninkhof, R.: Relationship between wind speed and gas exchange over the ocean revisited,
1024 *Limnology and Oceanography: Methods*, 12, 351–362, <https://doi.org/10.4319/lom.2014.12.351>,
1025 2014.
- 1026 Wanninkhof, R. and McGillis, W. R.: A cubic relationship between air-sea CO₂ exchange and
1027 wind speed, *Geophysical Research Letters*, 26, 1889–1892,
1028 <https://doi.org/10.1029/1999GL900363>, 1999.
- 1029 Wanninkhof, R., Park, G.-H., Takahashi, T., Sweeney, C., Feely, R., Nojiri, Y., Gruber, N.,
1030 Doney, S. C., McKinley, G. A., Lenton, A., Le Qu r , C., Heinze, C., Schwinger, J., Graven, H.,

- 1031 and Khatiwala, S.: Global ocean carbon uptake: magnitude, variability and trends,
1032 *Biogeosciences*, 10, 1983–2000, <https://doi.org/10.5194/bg-10-1983-2013>, 2013.
- 1033 Waycott, M., Duarte, C. M., Carruthers, T. J. B., Orth, R. J., Dennison, W. C., Olyarnik, S.,
1034 Calladine, A., Fourqurean, J. W., Heck, K. L., Hughes, A. R., Kendrick, G. A., Kenworthy, W.
1035 J., Short, F. T., and Williams, S. L.: Accelerating loss of seagrasses across the globe threatens
1036 coastal ecosystems, *Proceedings of the National Academy of Sciences*, 106, 12377–12381,
1037 <https://doi.org/10.1073/pnas.0905620106>, 2009.
- 1038 Weiss, R. and Price, B.: Nitrous oxide solubility in water and seawater, *Marine Chemistry*, 8,
1039 347–359, [https://doi.org/10.1016/0304-4203\(80\)90024-9](https://doi.org/10.1016/0304-4203(80)90024-9), 1980.
- 1040 Winslow, L. A., Zwart, J. A., Batt, R. D., Dugan, H. A., Woolway, R. I., Corman, J. R., and
1041 Read, J. S.: LakeMetabolizer: An R package for estimating lake metabolism from free-water
1042 oxygen using diverse statistical models, *Inland Waters*, 6, <https://doi.org/10.1080/IW-6.4.883>,
1043 2016.
- 1044 Xiao, S., Liu, L., Wang, W., Lorke, A., Woodhouse, J., and Grossart, H.-P.: A Fast-Response
1045 Automated Gas Equilibrator (FaRAGE) for continuous in situ measurement of CH₄ and CO₂
1046 dissolved in water, *Hydrology and Earth System Sciences*, 24, 3871–3880,
1047 <https://doi.org/10.5194/hess-24-3871-2020>, 2020.
- 1048 Zeebe, R. E. and Wolf-Gladrow, D.: CO₂ in Seawater: Equilibrium, Kinetics, Isotopes, Gulf
1049 Professional Publishing, 382 pp., 2001.
- 1050

1051 **Supplemental**

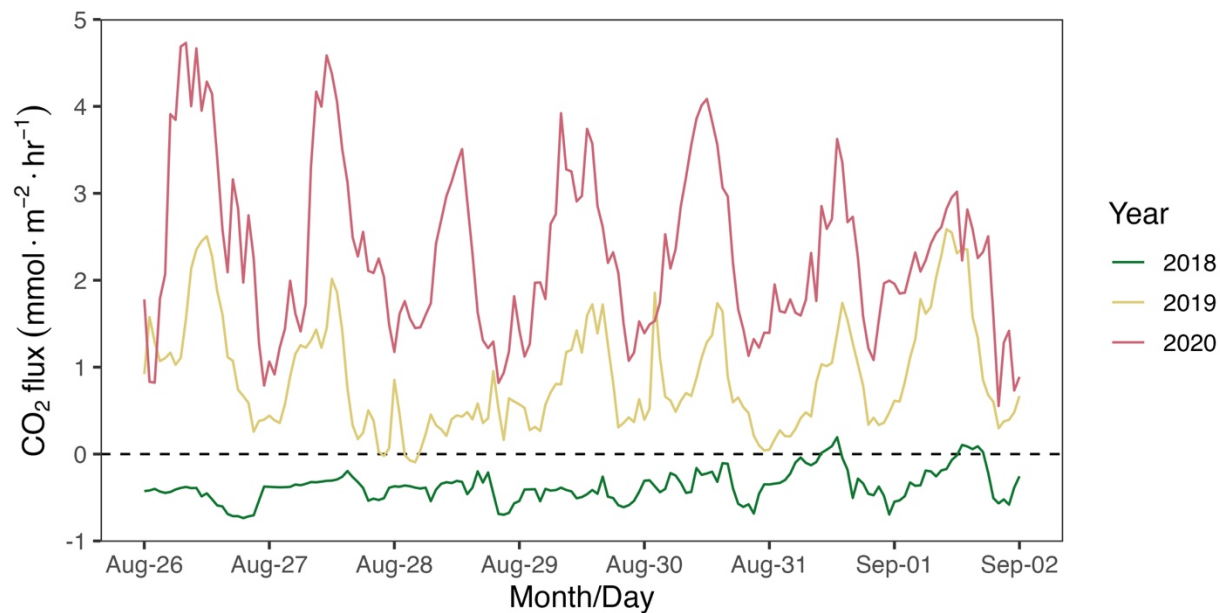


1052 **Fig. S1.** Plot of all raw values from environmental variables for the same time period as CO₂ flux
 1053 (July 2018–July 2021).
 1054

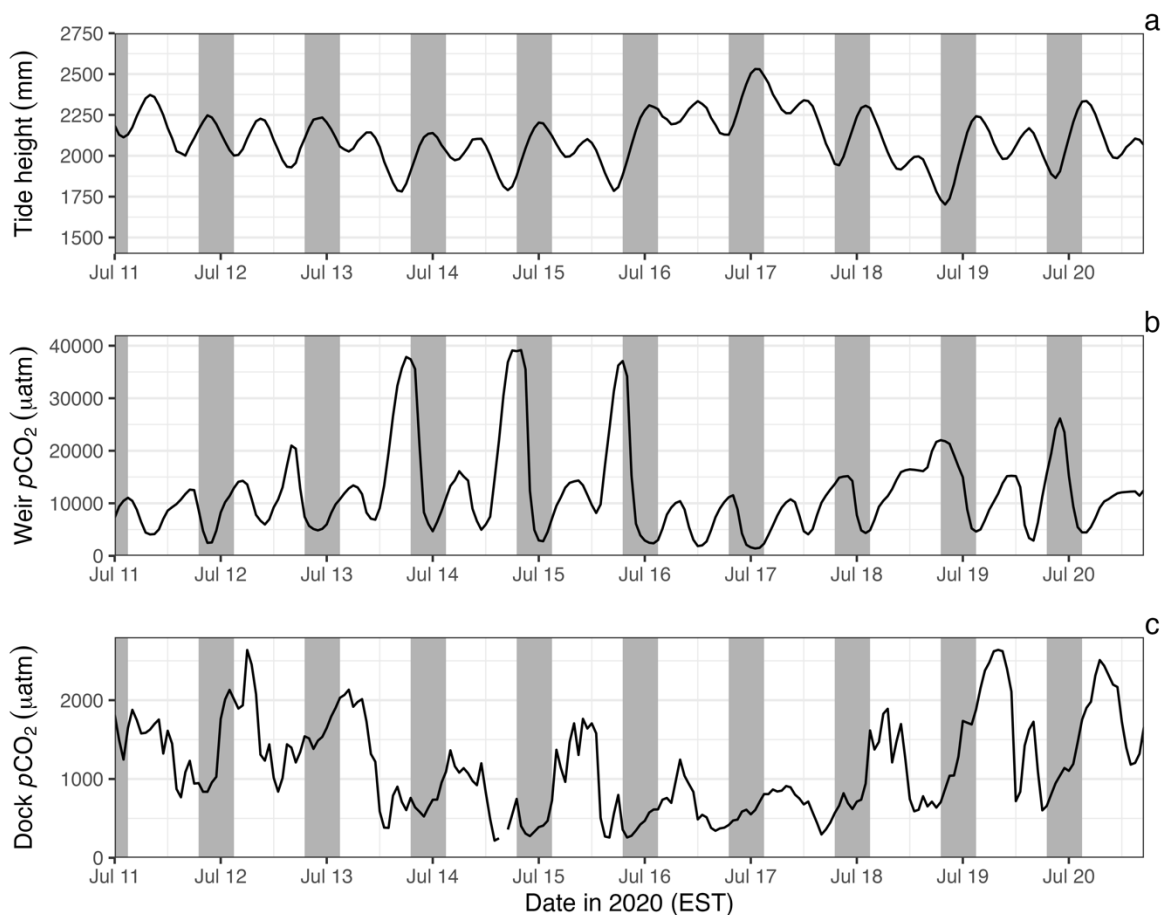


1056 **Fig. S2.** Average hourly values (95% CI) of environmental variables across 24 hours of the day
 1057 (July 2018–July 2021) in cold and warm seasons. Light/dark background indicates day/night
 1058 conditions.

1059
 1060



1061 **Fig. S3.** Hourly CO₂ flux estimates for the week of August 26 to September 2 where CO₂ flux
 1062 status differs among years.
 1063
 1064



1065
 1066 **Fig. S4.** Simultaneous $p\text{CO}_2$ measurements (1 hr intervals) from SERC dock (panel c) and the
 1067 mouth of the single tidal creek that drains the Kirkpatrick Marsh (panel b) (11–20 Jul 2020)
 1068 indicate that dissolved CO_2 varies at the dock according to a day/night cycle while CO_2 in the
 1069 marsh tidal creek rises and falls inversely with tide height (panel a), indicating outwelling of
 1070 marsh derived CO_2 (e.g., root respiration, pore and groundwater).